

1 **Wind, waves, and fronts: Frictional effects in a generalized Ekman model**

2 Jacob O. Wenegrat*

3 *University of Washington, Seattle, Washington*

4 Michael J. McPhaden

5 *Pacific Marine Environmental Laboratory, NOAA, Seattle, WA*

6 *Corresponding author address: School of Oceanography, University of Washington, Seattle, WA.

7 E-mail: wenegrat@uw.edu

ABSTRACT

8 Ocean currents in the surface boundary layer are sensitive to a variety of pa-
9 rameters not included in classic Ekman theory, including the vertical structure
10 of eddy viscosity, finite boundary layer depth, baroclinic pressure gradients,
11 and surface waves. These parameters can modify the horizontal and verti-
12 cal flow in the near-surface ocean, making them of first-order significance
13 to a wide range of phenomenon of broad practical and scientific import. In
14 this work, an approximate Green's function solution is found for a model of
15 the frictional ocean surface boundary layer, termed the generalized Ekman
16 (or Turbulent Thermal Wind) balance. The solution admits consideration of
17 general, more physically realistic, forms of parameters than previously possi-
18 ble, offering improved physical insight into the underlying dynamics. Closed
19 form solutions are given for the wind-driven flow in the presence of Coriolis-
20 Stokes shear, a result of the surface wave field, and thermal wind shear, arising
21 from a baroclinic pressure gradient, revealing the common underlying phys-
22 ical mechanisms through which they modify currents in the ocean boundary
23 layer. These dynamics are further illustrated by a case study of an idealized
24 two-dimensional front. The solutions, and estimates of the global distribution
25 of the relative influence of surface waves and baroclinic pressure gradients
26 on near-surface ocean currents, emphasize the broad importance of consider-
27 ing ocean sources of shear and physically realistic parameters in the Ekman
28 problem.

29 **1. Introduction**

30 Diagnosing velocities in the ocean boundary layer is key to many issues of broad practical and
31 scientific importance, from larval dispersion, to search and rescue, to the general ocean circulation.
32 Today much of our understanding of boundary layer currents remains rooted in classic Ekman
33 theory, which holds that, with some knowledge of the turbulent eddy viscosity, the ageostrophic
34 ocean response is completely determined by the surface wind stress (Ekman 1905). However,
35 despite the tremendous explanatory power of Ekman theory, basic observational confirmation of
36 the structure of flow in the boundary layer has been challenging.

37 In response to discrepancies between the theory and observations, a large literature has devel-
38 oped, focused on modifications to the classic Ekman theory. Broadly speaking the proposed mod-
39 ifications to Ekman theory can be divided into local one-dimensional mechanisms, such as time-
40 variability (Price et al. 1986; Schudlich and Price 1998; Price and Sundermeyer 1999; McWilliams
41 et al. 2009), vertical structure in eddy viscosity (Madsen 1977; Miles 1994; Grisogono 1995), or
42 finite boundary layer depth (Welander 1957; Stommel 1960; Lewis and Belcher 2004; Elipot and
43 Gille 2009), and mechanisms that involve non-local effects such as horizontal buoyancy gradi-
44 ents (McPhaden 1981; Cronin and Kessler 2009), surface waves (Huang 1979; Jenkins 1986; Xu
45 and Bowen 1994; Lewis and Belcher 2004; Polton et al. 2005), and non-linearity (Stern 1965;
46 Niiler 1969; Thomas and Rhines 2002). Many of these proposed modifications have closed the
47 gap between theory and observations, however, generally analytic solutions are only available for
48 specific forms of parameters, limiting the possibility for inter-comparison of the various proposed
49 mechanisms, and critically, their application to realistic ocean fields.

50 Here we utilize a simple model of the viscous boundary layer, termed the generalized Ekman
51 model (Cronin and Kessler 2009), or the Turbulent Thermal Wind balance (Gula et al. 2014). This

52 model contains many of the modifications to basic Ekman theory that have been proposed individ-
53 ually, and has already proven successful in explaining observed horizontal currents (Cronin and
54 Kessler 2009), as well as modeled boundary layer vertical velocities (Gula et al., McWilliams et
55 al., 2015). Previously, solutions to this model with physically realistic parameters required numer-
56 ical methods, with analytic solutions available only for greatly simplified forms of the parameters
57 (Bonjean and Lagerloef 2002; Cronin and Kessler 2009; McWilliams et al. 2015), limiting insight
58 into the underlying dynamics.

59 In this manuscript we significantly extend these earlier results by providing an approximate so-
60 lution to the generalized Ekman (Turbulent Thermal Wind) model that can accommodate a wide-
61 range of physically realistic parameters, providing a unifying framework for many of the individu-
62 ally proposed modifications to classic Ekman theory (section 2). Using this solution, two limiting
63 cases, corresponding to a surface wave field and horizontal buoyancy gradient, are explored to
64 further illuminate the underlying dynamics (section 3). The approximate solutions to these lim-
65 iting cases reveal how these two ocean dynamic processes modify the Ekman solution in similar
66 ways, drawing a previously unnoted connection between these processes, and their accompanying
67 literatures.

68 In section 4 the solution is applied to an idealized front, illustrating how thermal wind shear
69 in the presence of viscosity can alter both the Ekman layer flow as well as drive overturning
70 circulations in the boundary layer (Garrett and Loder 1981; Thompson 2000; McWilliams et al.
71 2015). Estimates of the global distribution of wave and baroclinic pressure gradient effects on
72 frictional boundary layer flow (section 5), and scaling analysis, suggest that these ocean dynamical
73 processes can be expected to be of first order importance in determining near-surface currents for
74 much of the world's oceans.

75 **2. Theory**

76 We consider steady, Boussinesq, flow in hydrostatic balance, where the complex horizontal ve-
 77 locity is denoted by $\mathbf{u} \equiv u + iv$, and $\nabla \equiv \frac{\partial}{\partial x} + i \frac{\partial}{\partial y}$. Horizontal mixing is ignored, and vertical
 78 mixing is parameterized by a turbulent eddy viscosity, A_v , which is considered to be a specified
 79 parameter, allowed to vary vertically subject to moderate constraints imposed by the approxima-
 80 tion technique utilized, as discussed below. The horizontal and vertical momentum equations are
 81 thus given by,

$$if\mathbf{u} = -\frac{1}{\rho_0}\nabla P + \frac{\partial}{\partial z}\left(A_v\frac{\partial\mathbf{u}}{\partial z}\right), \quad (1)$$

82

$$0 = -\frac{1}{\rho_0}\frac{\partial P}{\partial z} + b. \quad (2)$$

83 Where the Rossby number, $\varepsilon = U/fL$, is assumed small, and therefore the non-linear advection
 84 terms are excluded. Equation (2) expresses the hydrostatic balance, where $b = -g\rho/\rho_0$ is the
 85 buoyancy, also considered to be a known quantity, allowed to vary in the horizontal and vertical.

86 Equation (1), a balance between the Coriolis acceleration, the pressure gradient force, and the
 87 turbulent diffusive flux divergence provides the basic starting point for Ekman theory. Deriving
 88 Ekman's 1905 result begins with a decomposition of the total velocity into a geostrophic velocity
 89 in balance with the pressure gradient force ($\mathbf{u}_g = i(\rho_0 f)^{-1}\nabla P$), and solving for the ageostrophic
 90 velocity ($\mathbf{u}_a = \mathbf{u} - \mathbf{u}_g$) in a boundary layer with characteristic thickness $h_{Ek} = \sqrt{2A_v/f}$, the
 91 Ekman depth, where it is assumed that A_v is vertically uniform and $\nabla b = 0$ (see for example
 92 Gill 1982, section 9.6). Equation (1) is a second order linear ordinary differential equation for
 93 velocity and so requires two boundary conditions on \mathbf{u} , given for the classic Ekman problem by
 94 $\rho A_v \partial \mathbf{u}_a / \partial z = \boldsymbol{\tau}_w$ at the surface, where $\boldsymbol{\tau}_w$ is the surface wind stress, and $\mathbf{u}_a \rightarrow 0$ as $z \rightarrow -\infty$.

95 Here we take a more general approach that does not require separating into geostrophic and
 96 ageostrophic components, by first vertically differentiating (1), and multiplying by $\rho_0 A_v(z)$ to
 97 form an equation for the stress, $\boldsymbol{\tau} = \rho_0 A_v(z) \partial \mathbf{u} / \partial z$, which we refer to as the generalized Ekman
 98 model (following Cronin and Kessler 2009),

$$A_v(z) \frac{\partial^2 \boldsymbol{\tau}}{\partial z^2} - if \boldsymbol{\tau} = \rho_0 A_v(z) \nabla b, \quad (3)$$

$$\boldsymbol{\tau}(0) = \boldsymbol{\tau}_w, \quad (4)$$

$$\boldsymbol{\tau}(-h) = 0. \quad (5)$$

101 The relationship of this model to various alternate Ekman layer formulations is discussed in
 102 detail by Cronin and Kessler (2009), however we further note that this is the same model termed
 103 the Turbulent Thermal Wind balance by Gula et al. (2014, and McWilliams et al. 2015) in their
 104 investigation of submesoscale cold filament dynamics.

105 The surface boundary condition, (4), is unchanged from the classic Ekman problem, however
 106 the bottom boundary condition, (5), is posed as a no-stress condition, applied at a finite depth
 107 $z = -h$, rather than the no-slip condition utilized in the classic Ekman problem. This formulation
 108 of the problem maintains the classic Ekman transport, even in the presence of geostrophic shear
 109 at the base of the layer (Cronin and Kessler 2009), and is applicable at low latitudes or in depth
 110 limited seas (Stommel 1960; Bonjean and Lagerloef 2002). The solution technique utilized below
 111 is a global method, as opposed to a local boundary layer expansion, and thus sufficiently far from
 112 the boundary layer the solution will approach the inviscid limit. This gives a measure of flexibility
 113 in the choice of an appropriate h , however on the basis of physical arguments, developed further
 114 below, h should be chosen to be deeper than significant sources of geostrophic stress (defined in
 115 section 3b), so as to avoid the creation of a spurious interior ‘Ekman’ layer. When $h \gg h_{Ek}$, as

116 is the case for most of the extra-tropics, the near-surface solution is insensitive to the particular
 117 bottom boundary condition, and we further note that for the solutions given below letting $h \rightarrow \infty$
 118 results in simplified forms of the solutions that are equivalent to applying the bottom boundary
 119 condition $\tau \rightarrow 0$ as $z \rightarrow -\infty$. However, if a no-slip boundary condition is desired, the derivation
 120 follows directly from that given in Appendix A.

121 To solve this linear inhomogeneous ordinary differential equation with non-constant coefficients,
 122 we first approximate a solution to the homogenous formulation of equation (3) using the Wentzel-
 123 Kramer-Brillouin (WKB) method (Bender and Orszag 1978; Grisogono 1995), and then solve for
 124 the inhomogeneous solution using variation of parameters (Hidaka 1955; Berger and Grisogono
 125 1998). A detailed derivation of the full solution is presented in Appendix A, however, briefly, the
 126 WKB method assumes the solution can be represented as:

$$\tau \propto e^{(S_0 + S_1 \delta + S_2 \delta^2 + \dots) \frac{1}{\delta}}. \quad (6)$$

127 Here, we use the physical optics approximation, and solve to first order (S_1). The distinguished
 128 limit for the small parameter δ is found to be $\delta \sim Ek^{1/2}$, where $Ek = A_v / fH^2$, the Ekman number.
 129 The classic non-dimensionalization of (1), for constant A_v , identifies H as the depth scale of the
 130 interior flow, which for values typical of a stratified mid-latitude ocean ($A_v \sim 10^{-2} \text{m}^2 \text{s}^{-1}$, $f \sim$
 131 10^{-4}s^{-1} , $H \sim 100 \text{m}$) gives $Ek \sim O(10^{-2})$. However, retaining vertical structure in A_v introduces
 132 an additional vertical length scale, h_{A_v} , into the problem. We thus have six physically relevant
 133 terms (A_v , f , u_g , u_a , H , h_{A_v}), with two physical dimensions (time and length). Application of the
 134 Buckingham pi theorem (Buckingham 1914) then gives 4 non-dimensional parameters, 2 of which
 135 take the form of an Ekman number, $\pi_1 = A_{v0} / fH^2$ and $\pi_2 = A_{v0} / fh_{A_v}^2$. The latter of these is likely
 136 to be a stricter constraint on the validity of the WKB expansion (Appendix B).

137 Formally, the use of the WKB approximation requires that the properties of the medium vary
138 more slowly than the solution (Bender and Orszag 1978), a condition which may be violated in
139 some geophysical flows. Further analysis of this requirement is given in Appendix A, however,
140 as discussed in Appendix B, we find good agreement between numerical and approximate solu-
141 tions for a range of A_v profiles, and values of Ek , suggesting the utility of this solution (see also
142 Grisogono 1995). For simplicity we also require that $A_v > 0$ throughout the layer, so as to avoid
143 the additional complexity of singularities in the equation. This constraint, and the WKB condition
144 (A12), does not allow the direct application of the solution to cases where $A_v \rightarrow 0$ as $z \rightarrow 0$, as
145 for instance occurs in the K-Profile Parameterization (KPP) (Large et al. 1994). If necessary, this
146 restriction can be removed by patching the WKB solution to an inner solution, valid in a thin layer
147 as $A_v \rightarrow 0$ (as in Parmhed et al. 2005), discussed further in Appendix B.

148 Once the WKB solution to the homogenous problem is identified, the inhomogeneous solution
149 can be found using variation of parameters, and stated in terms of a Green's function. The full
150 solution (as derived in Appendix A) is thus given by,

$$\tau(z) = \tau_w \left(\frac{A_v(z)}{A_v(0)} \right)^{\frac{1}{4}} \frac{\sinh[\theta(z)]}{\sinh[\theta(0)]} + \int_{-h}^0 G(z, s) [\rho_0 \nabla b] ds. \quad (7)$$

151 Where,

$$\theta(z) = \sqrt{if} \int_{-h}^z A_v(Z)^{-\frac{1}{2}} dZ, \quad (8)$$

152 and, $G(z, s)$ is the symmetric Green's function,

$$G(z, s) = \begin{cases} \frac{\sinh[\theta(z)] \sinh[\theta(s) - \theta(0)] A_v(s)^{\frac{1}{4}} A_v(z)^{\frac{1}{4}}}{\sinh[\theta(0)] \sqrt{if}} & \text{if } s > z \\ \frac{\sinh[\theta(s)] \sinh[\theta(z) - \theta(0)] A_v(s)^{\frac{1}{4}} A_v(z)^{\frac{1}{4}}}{\sinh[\theta(0)] \sqrt{if}} & \text{if } s < z. \end{cases} \quad (9)$$

153 This general solution is a primary result of this manuscript.

154 Velocity shear follows directly from the definition of stress. However, equation (3) is a third-
155 order linear ordinary differential equation in velocity, and hence to go from shear to velocity

156 requires an additional boundary condition. Here, to determine velocity we use the solution for
 157 stress directly in the momentum equation (1),

$$if\mathbf{u} = -\frac{1}{\rho}\nabla P + \frac{1}{\rho}\frac{\partial\boldsymbol{\tau}}{\partial z}, \quad (10)$$

158 where $\boldsymbol{\tau}$ is now known through (7). This approach ensures that the vertically integrated
 159 ageostrophic velocity satisfies the classic Ekman transport relation.

160 *a. Wind-Driven Component*

161 The wind-driven component of the stress is given by the first term on the RHS of (7), which
 162 can be compared to the exact solution for the case where A_v is vertically constant (Stommel 1960;
 163 Bonjean and Lagerloef 2002),

$$\boldsymbol{\tau}(z) = \boldsymbol{\tau}_w \frac{\sinh\left[\sqrt{\frac{if}{A_v}}(z+h)\right]}{\sinh\left[\sqrt{\frac{if}{A_v}}h\right]}. \quad (11)$$

164 The parallels between the WKB approximation, (7), and the solution of the constant- A_v problem
 165 (11) are apparent, with the leading order modification appearing in the argument of the hyperbolic
 166 functions, $\theta(z)$, given by (8). This term can be understood as introducing a stretched vertical
 167 coordinate system, defined by the integral in (8) (Lupini et al. 1975). Accordingly, $h_{Ek}(z) =$
 168 $\sqrt{2A_v(z)/f}$ defines a vertically localized Ekman depth, analogous to the local wavenumber found
 169 in WKB solutions to the wave equation (see for example Gill 1982, section 8.12).

170 The amplitude of the stress is also modified by vertical variations in viscosity, which appears as a
 171 ratio to the $1/4$ power. For a slowly vertically decaying A_v , the effect of this term will be apparent
 172 only as $z \rightarrow -h$, where the ratio of $A_v(z)/A_v(0) \ll 1$. Figure 1 compares example vertical profiles
 173 of stress and velocity for the case of A_v decaying exponentially with depth, and for constant A_v ,
 174 to illustrate the modification of the vertical structure arising from retaining a depth-dependent
 175 A_v . This depth dependent amplitude term allows the stress amplitude, and hence the ageostrophic

176 velocity, to decay over a different vertical depth scale than the rotation of the stress vector, a
177 feature which is commonly noted in observations but cannot be accommodated in classic Ekman
178 theory (Price et al. 1986; Wijffels et al. 1994; Chereskin 1995; Price and Sundermeyer 1999). It is
179 apparent that if A_v is vertically constant in (7), the standard solution (11), as originally identified by
180 Stommel (1960) in an investigation of the dynamics of the equatorial undercurrent, is immediately
181 recovered.

182 *b. Inhomogenous Forcing*

183 The second term on the RHS of (7) is a Green's function integral, which can accommodate
184 arbitrary vertical structure in both ocean sources of stress, which appear as inhomogenous forcing
185 terms in (3), as well as in the profile of $A_v(z)$, subject only to the constraints imposed by the
186 WKB method. The Green's function kernel takes the form of paired Ekman layers above and
187 below interior sources of stress (figure 2), which demonstrates how ocean sources of shear in the
188 presence of viscosity drive an ageostrophic frictional response felt throughout the entire boundary
189 layer (Hidaka 1955; Csanady 1982). Far from the boundaries the profile of the Green's function
190 is symmetric above and below interior shear, however approaching the boundaries of the domain
191 the shape of the Green's function becomes increasingly asymmetric, and the integral contribution
192 serves to satisfy the boundary conditions (4) and (5).

193 The ageostrophic flow associated with several simplified forcings are shown in schematic form
194 in figure 3. In the absence of wind-stress, with vertically uniform A_v and ∇b , Ekman layers are
195 generated, both at the surface as well as at the base of the boundary layer, to satisfy the boundary
196 conditions (Bonjean and Lagerloef 2002). A more physically realistic case is given in figure 3b,
197 where a vertically decaying buoyancy gradient gives rise to both a surface Ekman layer, as well as
198 a diffuse interior ageostrophic flow. The strength of the interior portion of the flow, for the situation

199 shown in figure 3b, scales as h_{Ek}/h relative to the surface ageostrophic flow, and is therefore often
200 assumed small and neglected. However, we note that this flow is necessary to balance the transport
201 in the surface Ekman layer so as to maintain the classic Ekman transport relation. Further, this flow
202 need not always be small, as illustrated in section 3a discussing surface wave effects, and hence
203 should be retained. The final panel shows the case of a decaying A_v profile, with constant ∇b .
204 The resulting ageostrophic velocities are similar to those in figure 3b, however the associated
205 buoyancy fluxes will differ between the two cases, emphasizing how horizontal fluxes will be a
206 complex function of the spatial structure of both the background fields and A_v , discussed further
207 in section 5b.

208 The total frictional ageostrophic response thus consists of a directly wind-forced component, as
209 well as an integral over Ekman-like responses to interior shear. Therefore, in order to understand
210 the oceanic response to wind-forcing it is also necessary to understand the ageostrophic frictional
211 response to ocean dynamical processes (Cronin and Kessler 2009). Recent observational work
212 has emphasized the importance of removing estimates of the geostrophic shear in order to isolate
213 the ageostrophic flow (Chereskin and Roemmich 1991; Polton et al. 2013; Roach et al. 2015),
214 however the analysis developed here suggests that to fully isolate the wind-driven component of
215 this flow it is also necessary to account for ageostrophic flow driven by the geostrophic shear
216 (section 3b). Further, although we have so far limited the discussion to shear which arises from
217 baroclinic pressure gradients, we note that any other forcing terms in the momentum equations will
218 act in a similar manner, and the case of Stokes shear from surface waves is discussed in section 3a.
219 In order to further illustrate the underlying dynamical mechanisms we now consider two limiting
220 cases representing important sources of shear in the ocean surface boundary layer which admit
221 further simplification of the full solution.

222 3. Limiting Cases

223 *a. Stokes Shear: $h_s \ll h_{Ek}$*

224 Surface waves modify the oceanic boundary layer in a variety of important ways (Xu and Bowen
 225 1994; McWilliams et al. 1997; McWilliams and Restrepo 1999; Sullivan and McWilliams 2010;
 226 Belcher et al. 2012; McWilliams et al. 2012). Here we focus on one particular aspect, termed the
 227 Coriolis-Stokes force, which appears as an additional term in the Eulerian momentum equation that
 228 arises from rotation acting on the Stokes drift, leading to a tilting of wave-orbitals in the along-
 229 crest direction (Polton et al. 2005). The Coriolis-Stokes force has been shown to significantly
 230 modify flow in both the very near-surface layer, as well as throughout the entire Ekman layer
 231 (Huang 1979; Jenkins 1986; Lewis and Belcher 2004; Polton et al. 2005; Aiki and Greatbatch
 232 2012; McWilliams et al. 2014).

233 Equation (1) can be re-written to include the Coriolis-Stokes force as,

$$if(\mathbf{u} + \mathbf{u}_s) = -\frac{1}{\rho_0} \nabla P + \frac{\partial}{\partial z} \left(A_v \frac{\partial \mathbf{u}}{\partial z} \right), \quad (12)$$

234 with \mathbf{u}_s the Stokes velocity, given by, $\mathbf{u}_s(z) = \int_k 2\sigma k \chi(k) e^{2|k|z} dk$, and where σ is the wave fre-
 235 quency, k the wavenumber vector, and $\chi(k)$ the directional wave spectrum (Huang 1971). We make
 236 the common simplifying assumption that \mathbf{u}_s can be treated as a monochromatic wave such that
 237 $\mathbf{u}_s = U_0 e^{\frac{z}{h_s}} \hat{\mathbf{s}}(\mathbf{t})$, where $h_s = (2|k|)^{-1}$, and $\hat{\mathbf{s}}(\mathbf{t})$ is a unit vector in the direction of the waves, which
 238 is not necessarily aligned with the local surface wind stress. The wavenumber, k , and amplitude,
 239 U_0 are assumed to be known or parameterized. It is important to note that for a time-varying wave
 240 field, the Coriolis-Stokes force initially accelerates an ‘anti-Stokes’ flow (McWilliams and Fox-
 241 Kemper 2013), with transients that decay as $1/ft$ (Lewis and Belcher 2004). In the steady-state
 242 problem, including the Coriolis-Stokes force results in an additional forcing term on the RHS of
 243 (3), perpendicular to the wave direction, given by $if\rho A_v \partial \mathbf{u}_s / \partial z$. This appears in the full solution

244 (7) within the Green's function integral, replacing the bracketed term with, $[\rho \nabla b + i f \rho \partial \mathbf{u}_s / \partial z]$.
 245 Hence, both horizontal buoyancy gradients and Stokes shear modify the standard Ekman solution
 246 in mathematically identical ways.

247 In order to provide an asymptotic approximation to (7), we can take advantage of the scale
 248 separation between the typical depth scale of the surface waves, h_s , which is of order several
 249 meters, and h_{Ek} which is of order tens of meters, such that $h_s \ll h_{Ek}$. For simplicity in deriving the
 250 given form of (13), it is also assumed that $\tau_{CS}(-h) \sim 0$, and $h_{Av} \gg h_{Ek}$ where h_{Av} is the depth scale
 251 over which A_v varies, however neither of these assumptions are critical. After repeated integration
 252 by parts of (7) an asymptotic approximation is given by,

$$\tau(z) \sim [\tau_w - \tau_{CS}(0)] \left(\frac{A_v(z)}{A_v(0)} \right)^{\frac{1}{4}} \frac{\sinh[\theta(z)]}{\sinh[\theta(0)]} + \tau_{CS}(z), \quad \frac{h_s^2}{h_{Ek}^2} \rightarrow 0. \quad (13)$$

253 The surface wave field therefore introduces a Coriolis-Stokes stress,

$$\tau_{CS}(z) = -\rho A_v \frac{\partial \mathbf{u}_s}{\partial z} \left(1 + i \frac{1}{2} \frac{h_{Ek}^2(z)}{h_s^2} \right)^{-1}, \quad (14)$$

254 which is rotated $(90 + \Lambda)^\circ$ to the left of the wave direction (Northern Hemisphere) where $\Lambda \sim$
 255 $\tan^{-1}(h_s^2/h_{Ek}^2)$ (Figure 4). This stress modifies the ageostrophic frictional response in two ways.
 256 First, the Coriolis-Stokes stress can balance a portion of the applied surface wind stress, leading
 257 to a total Ekman layer response which can be considered as forced by an effective stress, given
 258 by the first bracketed term on the RHS of (13), rather than by the wind stress alone (Polton et al.
 259 2005; McWilliams et al. 2014). Second, the Coriolis-Stokes stress directly affects a layer of depth
 260 scale h_s , through the last term on the RHS of (13). The vertical divergence of this term, in (12),
 261 drives near-surface ageostrophic velocities that tend to rotate the surface flow into the down-wave
 262 direction (Fig. 4b,c). Together these two modifications introduce a boundary layer transport of
 263 $-U_0 h_s$, canceling the Lagrangian Stokes transport (see Polton et al. 2005, for a detailed discussion
 264 of the frictional Coriolis-Stokes transport).

265 The results of this section confirm the analysis of Polton et al. (2005), and extend them to an ar-
 266 bitrary vertical structure of A_v , subject to the aforementioned constraints. As discussed by Polton
 267 et al. (2005, their section 2c), (13) and (14) imply that in the limit $h_s^2/h_{Ek}^2 \rightarrow 0$, the wave modifica-
 268 tion to the Eulerian currents can be modeled solely through a modification to the surface boundary
 269 condition. The proceeding analysis confirms this result is fully independent of the particular form
 270 of vertical mixing, and consequently may be of general use in guiding observational or modeling
 271 studies where the Stokes layer is not directly resolved.

272 *b. Thermal wind shear: $h_{Ek} \ll h_\rho, h_{Av}$*

273 A similar simplification of Eq. (7) can be found for the case of a horizontal buoyancy gradi-
 274 ent driving a thermal wind shear in the near-surface layer. We assume that the Ekman depth is
 275 shallow relative to the depth scales over which the horizontal density gradient and A_v vary, ie.
 276 $h_{Ek} \ll h_\rho, h_{Av}$. An example of the scales associated with a mesoscale frontal system can be found
 277 from observations of the Azores front (Rudnick 1996), where, using parameters from Nagai et al.
 278 (2006), $h_{Ek} \sim 15$ m, $h_{Av} \sim 40$ m, based on the depth of the transition layer below the mixed layer,
 279 and $h_\rho \sim 100$ m, based on the depth of the thermocline and the observed geostrophic frontal veloc-
 280 ity. This limiting case is marginally valid for these parameter values, and thus can be considered
 281 as requiring a fairly idealized frontal configuration (cf. Thomas and Lee 2005), included largely
 282 for the insight it offers into the basic dynamics of (7), and for comparison with (13).

283 For simplicity it is also assumed that $A_v \nabla b \rightarrow 0$ at $z = -h$. If this assumption is not made
 284 the solution requires an additional bottom Ekman layer at $z = -h$ in order to satisfy the bottom
 285 boundary condition (5), as shown schematically in Fig. 3a. Repeated integration by parts of

286 equation (7) leads to an asymptotic approximation given by,

$$\tau(z) \sim [\tau_w - \tau_{geo}(0)] \left(\frac{A_v(z)}{A_v(0)} \right)^{\frac{1}{4}} \frac{\sinh[\theta(z)]}{\sinh[\theta(0)]} + \tau_{geo}(z), \quad \frac{h_{Ek}^2}{h_{\rho, A_v}^2} \rightarrow 0. \quad (15)$$

287 Where,

$$\tau_{geo}(z) = \rho A_v \frac{\partial \mathbf{u}_g}{\partial z} \left(1 - ih_{Ek}^2(z) \left[\frac{A'_v}{A_v} \frac{\nabla b'}{\nabla b} + \frac{1}{2} \frac{\nabla b''}{\nabla b} + \frac{3}{8} \frac{A''_v}{A_v} + \frac{3}{32} \left(\frac{A'_v}{A_v} \right)^2 \right] \right), \quad (16)$$

288 defines the geostrophic stress, with primes denoting vertical differentiation.

289 Closely paralleling the solution for the Coriolis-Stokes stress, (13), the modification of the sur-
 290 face boundary layer stress by horizontal buoyancy gradients also consists of two components. The
 291 first is a modification to the Ekman layer, whereby the Ekman response is forced only by that
 292 portion of the wind stress that is out of balance with the geostrophic stress, which again can be
 293 considered as defining an effective surface stress, given by the first bracketed term on the RHS
 294 of equation (15) (Thompson 2000; Nagai et al. 2006; Cronin and Kessler 2009). Thus, even in
 295 the case of $\tau_w = 0$, thermal wind shear will drive an ageostrophic flow within the Ekman layer,
 296 with implications for frontal spin-down (Garrett and Loder 1981; Csanady 1982; Thompson 2000;
 297 Thomas and Rhines 2002), filament frontogenesis (Gula et al. 2014; McWilliams et al. 2015), and
 298 near-surface fluxes (Thomas and Ferrari 2008), discussed in section 5b. It is worth noting that
 299 advection of the horizontal buoyancy gradient by the ageostrophic frictional flow can modify the
 300 buoyancy gradient and thereby feedback into the Ekman solution, which is discussed in further
 301 detail in Thompson (2000), and McWilliams et al. (2015).

302 The second term on the RHS of equation (15) represents the turbulent stress that arises directly
 303 from a thermal wind shear in the presence of a viscosity, often termed the geostrophic stress, given
 304 by (16). The divergence of this term drives a weak flow throughout the entire layer with velocities
 305 that scale as h_{Ek}/h relative to the ageostrophic velocity in the Ekman layer, but with a vertically

306 integrated transport that exactly cancels the transport in the Ekman layer driven by the surface
 307 geostrophic stress. The definition of geostrophic stress given here, (16), differs from that given
 308 by previous investigators, who, considering only vertically uniform A_v and ∇b , suggest $\tau_{geo}(z) =$
 309 $\rho A_v \frac{\partial \mathbf{u}_g}{\partial z}$. Including vertical structure in these parameters gives rise to four additional terms in the
 310 definition of geostrophic stress, bracketed in (16), which enter the asymptotic approximation at
 311 order $h_{Ek}^2/h_{\rho,Av}^2$.

312 These additional terms are imaginary, and thus have the effect of rotating the geostrophic
 313 stress vector slightly from the geostrophic shear vector. This is illustrated in figure 5, where
 314 the geostrophic stress vector is rotated by an angle, λ , which scales as $\lambda \sim \tan^{-1}(h_{Ek}^2/h_{\rho,Av}^2)$,
 315 or equivalently, $\lambda \sim \tan^{-1}(2Ek)$ (figure 6). Transport in the Ekman layer, U_{Ek}^T , is opposed by
 316 geostrophic stress driven transport over the full boundary layer depth, U_{BL}^T . Surface velocity is
 317 given by $u_{surf} = u_{Ek}(0) + u_{BL}(0)$, a combination of the Ekman ageostrophic velocity forced by
 318 the effective surface stress (u_{Ek}), and an interior ageostrophic velocity forced by the divergence of
 319 the geostrophic stress (u_{BL}). The direction of the near-surface frictional flow relative to the buoy-
 320 ancy gradient is consequently a function of both the angle of the geostrophic stress, determined
 321 by vertical structure in A_v and ∇b , as well as the ratio $u_{BL}/u_{Ek} \sim h_{Ek}/h$. As a corollary to this,
 322 a latitudinal dependence in λ appears implicitly through the Ekman depth, as $h_{Ek}^2/h_{\rho,Av}^2 \rightarrow \infty$ as
 323 $f \rightarrow 0$, with the geostrophic stress vector becoming increasingly parallel to the buoyancy gradient
 324 at low latitudes.

325 4. Frictional Secondary Circulation

326 The cross front circulation which arises from frictional effects, shown schematically in figure 3,
 327 acts to spin-down ocean fronts, and sharpen cold filaments, due to buoyancy fluxes associated with
 328 the ageostrophic velocities necessary to match the surface boundary condition, (4), in the presence

329 of a geostrophic shear (Garrett and Loder 1981; Thompson 2000; McWilliams et al. 2015). Fur-
 330 ther, in the case that $\nabla^2 b \neq 0$, convergences (divergences) of this cross-front ageostrophic circu-
 331 lations will drive negative (positive) vertical velocities in the boundary layer (Garrett and Loder
 332 1981; Thompson 2000). These effects have been examined primarily in the context of subme-
 333 soscale dynamics, where the Rossby number, ε , is not small, and hence are generally diagnosed
 334 within the context of non-linear models (eg. Nagai et al. 2006). However, recent comparisons with
 335 modeled submesoscale eddies and filaments have suggested that vertical velocities in the bound-
 336 ary layer can be accurately diagnosed using this simple linear theory even at high ε (Ponte et al.
 337 2013; Gula et al. 2014; McWilliams et al. 2015). At larger spatial scales, similar effects are also
 338 suggested in an ocean global climate model (Cronin and Tozuka 2015). Therefore, friction acting
 339 on the baroclinic component of the flow may be important to boundary layer dynamics across a
 340 range of spatial scales.

341 Vertical velocity for the generalized Ekman model is given by the standard relationship,

$$w(x, y, z) = -\hat{k} \cdot \nabla \times \frac{\boldsymbol{\tau}(x, y, z)}{\rho f} + L(x, y), \quad (17)$$

342 where $L(x, y)$ is a constant of vertical integration chosen to fulfill a rigid lid boundary condition.
 343 To illustrate how the various components of the full solution enter the calculated vertical velocity
 344 we can utilize the simplified definition of stress given by (13), and (15), in (17), which for a two
 345 dimensional configuration, invariant in the y -direction, reduces to,

$$w(x, z) = -\frac{\partial}{\partial x} \left[\text{Im} \left\{ \frac{\boldsymbol{\tau}_{Eff}(x)}{\rho f} \left(\frac{A_v(x, z)}{A_v(x, 0)} \right)^{\frac{1}{4}} \frac{\sinh[\boldsymbol{\theta}(x, z)]}{\sinh[\boldsymbol{\theta}(x, 0)]} \right\} \right] - \frac{\partial}{\partial x} \left[\text{Im} \left\{ \frac{\boldsymbol{\tau}_{Int}(x, z)}{\rho f} \right\} \right] + L(x). \quad (18)$$

346 The first term on the RHS represents upwelling occurring within the Ekman layer, which is
 347 now forced by an effective stress, $\boldsymbol{\tau}_{Eff} = \boldsymbol{\tau}_w - \boldsymbol{\tau}_{CS}(0) - \boldsymbol{\tau}_{geo}(0)$. The second term on the RHS
 348 gives the boundary layer vertical velocity arising solely from the gradient of the interior forcing,

349 $\tau_{Int} = \tau_{CS} + \tau_{geo}$. When (18) is evaluated at the base of the layer, $z = -h$, it reduces to the
 350 classic Ekman upwelling driven solely by the curl of the wind-stress, however, within the layer,
 351 both horizontal gradients in the forcing and horizontal gradients of the vertical structure can drive
 352 vertical velocities. For the Ekman layer, this can be envisioned as Ekman transport occurring along
 353 contours of constant h_{Ek} , which, for a spatially varying A_v , have a vertical component.

354 Below the surface Ekman layer, where $\tau_{CS}(x, z) \approx 0$, and in the limit of $h_{Ek}^2/h_{\rho, A_v}^2 \rightarrow 0$, (18)
 355 reduces to the scaling given by Garrett and Loder (1981), $w \sim gf^{-2}\rho^{-1}\partial(A_v\partial\rho/\partial x)/\partial x$. Thus,
 356 vertical velocity in the boundary layer interior, outside the Ekman layer, is driven by gradients in
 357 thermal wind shear and A_v , with order $h_{Ek}^2/h_{\rho, A_v}^2$ modifications due to the gradient of the bracketed
 358 terms in (16), reflecting the role of the vertical structure of A_v and ∇b in setting the direction of
 359 the geostrophic stress vector (Section 3b, figure 6). Approaching the surface, vertical velocity
 360 decays exponentially over an Ekman layer of depth scale h_{Ek} , with additional near-surface vertical
 361 velocities in a thin layer of depth scale h_s driven by the horizontal divergence of the Coriolis-Stokes
 362 stress.

363 To illustrate the secondary circulation that arises from the balance (1), we examine an idealized
 364 front in the x - z plane (200 km width, $h=500$ m), based on an approximation of the Frontal Air-Sea
 365 Interaction Experiment (FASINEX) data (Pollard and Regier 1992), similar to Thompson (2000).
 366 We set $\tau_w = 0$ and $\tau_{CS} = 0$ as the solution is linear and these effects are simply additive. The
 367 buoyancy in this model is given by,

$$b(x, z) = \frac{1}{2}b_f \tanh \left[\frac{\hat{z} - \alpha(\hat{x} - x_0)^3 - z_0}{d_0} \right] + \frac{1}{2}b_b \tanh \left[\frac{\hat{z} - z_0}{d_1} \right], \quad (19)$$

368 with values of parameters given in Table 1 and the hat notation indicating non-dimensionalized
 369 coordinates ranging from 0 to 1. Values of A_v are based on the approximation used in McWilliams
 370 et al. (2015), designed to be broadly consistent with KPP (Large et al. 1994). This is used simply

371 to illustrate several general features of the solution that arise from horizontal and vertical structure
 372 in mixing across a frontal region, rather than provide an absolutely accurate diagnostic, and the
 373 qualitative discussion that follows is not sensitive to the detailed particulars of our choice of A_v .

$$A_v(x, z) = A_{v0}G(\zeta)\frac{\hat{h}(\hat{x})}{h_0} + A_{vb}, \quad \zeta = -\frac{\hat{z}}{\hat{h}(x)}, \quad (20)$$

$$G(\zeta) = \frac{27}{4}(1 + \zeta_0^2)(\zeta_0 + \zeta)(1 - \zeta)^2, \quad \zeta \leq 1, \quad (21)$$

$$G(\zeta) = 0, \quad \zeta > 1. \quad (22)$$

376 G has a maximum value of 1 in the boundary layer, ζ_0 is a small parameter introduced to avoid a
 377 singularity at $z = 0$, and \hat{h} is the surface boundary layer depth, taken here as,

$$\hat{h}(x) = h_0 + \delta_h \left(\tanh \left[\frac{\alpha(\hat{x} - x_0)^3}{d_0} \right] - \frac{1}{2} \right). \quad (23)$$

378 All parameter values for equations (19-23) are given in Table 1. Figure 7 shows the structure of
 379 the idealized front, and the eddy viscosity, along with the associated along front geostrophic flow,
 380 implying $\varepsilon \sim 0.05$. We further assume $w = 0$ at $z = 0$ (rigid lid), and define an ageostrophic cross-
 381 front streamfunction such that $(u_{ag}, w) = (\psi_z, -\psi_x)$. Using the meridional momentum equation,
 382 Im[Eq. (1)], gives

$$\psi = \frac{1}{\rho f} \tau^y(x, z). \quad (24)$$

383 The secondary overturning circulation arising from the geostrophic stress is found numerically,
 384 and shown in figure 7. This is a thermally direct circulation, with a counter-clockwise sense of
 385 rotation, that tends to tilt the front and restratify the near-surface (Thompson 2000). Downwelling
 386 velocities on the dense side of the front are stronger than the upwelling on the buoyant side of the
 387 front, consistent with previous findings (Samelson 1993; Thompson 2000). Streamlines are closed,
 388 indicating zero vertically integrated horizontal transport, as required to maintain the classic Ekman

389 transport. This is a general result that does not depend on the frontal configuration. Note however
 390 that although the vertically integrated horizontal transport is zero, the associated fluxes need not
 391 be zero, as discussed further in section 5b. Further, the vertical buoyancy flux associated with the
 392 secondary overturning circulation can be non-zero (McWilliams et al. 2015), and hence may play
 393 a role in the general circulation through vorticity stretching of the interior.

394 To illustrate the importance of spatial variability in A_v , we decompose the total vertical velocity
 395 field (figure 8a), w_{total} , into vertical velocities due to the gradient in the forcing ($\nabla^2 b$), which we
 396 designate $w_{forcing}$, and the remainder which is a function only of the spatial structure in A_v , which
 397 we designate w_{Av} , as discussed in relation to (18). For the particular frontal configuration examined
 398 here w_{Av} is $\sim 25\%$ of w_{total} . However, locally near the base of the turbulent boundary layer (Fig 8,
 399 dashed line) w_{Av} can be the dominant term, and hence may be of particular importance for vertical
 400 fluxes into the near-surface layer. For a geostrophic stress, the ratio of vertical velocities is given
 401 by,

$$\frac{w_{Av}}{w_{forcing}} \sim \frac{L_{forcing}}{L_{Av}}, \quad (25)$$

402 where L indicates the relevant horizontal length scales. Observations suggest that horizontal length
 403 scales over which vertical mixing varies are comparable to frontal features (Dewey and Moum
 404 1990; Nagai et al. 2006), and hence these effects may be first order in determining the vertical
 405 velocity in the boundary layer. A similar scaling holds within the Ekman layer, where for a surface
 406 wind stress aligned orthogonal to a horizontal gradient in A_v , the ratio of vertical velocities at
 407 $z = -h_{Ek}$ is,

$$\frac{w_{Av}}{w_{forcing}} \sim \frac{L_{forcing}}{4L_{Av}}. \quad (26)$$

408 **5. Discussion and Further Implications**

409 The solutions presented here build upon prior work by allowing vertical variation in A_v , as well
410 as realistic structure in ocean fields, such as ∇b and the Coriolis-Stokes force. Examination of
411 the solutions (7, 13, 15), suggests many ways in which including more physical realism in the
412 problem parameters can modify the expected ageostrophic flow, however to further motivate the
413 importance of this added complexity, we first consider scaling arguments relating the importance
414 of geostrophic stress and Coriolis-Stokes stress to wind stress. The global distribution of these
415 fields are then estimated using a combination of model output and reanalysis data. Finally, we
416 comment briefly on the importance of these modifications to determining horizontal fluxes in the
417 boundary layer.

418 *a. Scaling and Geographic Distribution*

419 The boundary conditions utilized here ensure that the classic Ekman transport relation is main-
420 tained, even in the presence of ocean sources of stress. However, as demonstrated in Section 2,
421 ocean sources of stress can greatly modify the vertical structure of currents, and hence are fun-
422 damental to understanding boundary layer dynamics. Determining the magnitude of both the
423 geostrophic stress and the Coriolis-Stokes stress depends critically on the value of A_v , which
424 complicates their determination from observations. However, at low frequencies, variability in
425 near-surface A_v may be controlled by variability in the surface wind stress (Wenegrat et al. 2014).
426 Taking $h_{Ek} \sim u^*/f$ (Caldwell et al. 1972), where $u^* = \sqrt{\tau_w/\rho}$, gives $A_v \sim u^{*2}/f$, and hence the
427 ratio of the geostrophic stress to the surface wind stress can be scaled as,

$$\gamma_{GEO} = \frac{\tau_{geo}}{\tau_w} \sim \frac{\nabla b}{f^2}. \quad (27)$$

428 The direct proportionality of γ_{GEO} to ∇b , and independence from τ_w , highlights how the
 429 geostrophic stress can be expected to be a ubiquitous forcing of ageostrophic flow at sharp frontal
 430 features, and consequently may be fundamental for understanding horizontal heat flux at buoy-
 431 ancy fronts. The f^{-2} dependence indicates a rapid increase at low latitudes. Further, utilizing
 432 the stratified Ekman depth scaling, $h_{Ek} \sim u^*/\sqrt{Nf}$ (Pollard et al. 1973), in (27) gives $\gamma_{GEO} \sim Bu$,
 433 where $Bu = NH/fL$ is the Burger number, defined such that $b \sim N^2H$. Determination of Bu is thus
 434 dependent on the geometry of the particular front being considered, however, for many oceanic
 435 flows, observations suggest $Bu \sim O(1)$, implying $\gamma_{GEO} \sim O(1)$ (Nagai et al. 2006; Boccaletti et al.
 436 2007).

437 The Coriolis-Stokes stress can be scaled relative to the surface wind stress as,

$$\gamma_{CS} = \frac{\tau_{CS}}{\tau_w} \sim U_0 h_s \frac{\rho f}{\tau_w} \sim La^{-2} \frac{h_s}{h_{Ek}}. \quad (28)$$

438 Therefore, γ_{CS} is proportional to the Stokes transport divided by the wind-driven Ekman trans-
 439 port (McWilliams and Restrepo 1999; Polton et al. 2005). Alternatively, this can be rewritten using
 440 the turbulent Langmuir number, $La = (u^*/U_0)^{1/2}$, which scales the ratio of wind forced production
 441 of turbulent kinetic energy (TKE) to the wave forced production of TKE (McWilliams et al. 1997;
 442 Grant and Belcher 2009), with typical values of 0.2-0.5 (Smith 1992; Belcher et al. 2012). This
 443 suggests that $\gamma_{CS} \sim O(1)$ for h_s/h_{Ek} of 0.04 - 0.25.

444 To form estimates of the global distributions of γ_{GEO} and γ_{CS} a combination of reanalysis data
 445 and model output is utilized. The total Stokes transport is found from the WaveWatch III (WWIII)
 446 model, reported every 6 hours on a 0.5° grid (Rascle et al. 2008; Rascle and Ardhuin 2013). For
 447 consistency with the WWIII model forcing, we utilize NCEP Climate Forecast System Reanal-
 448 ysis (CFSR) wind stress, temperature and salinity at 5 m, and horizontal currents at 5 and 15 m
 449 depth (Saha et al. 2006). To estimate the geostrophic stress we calculate buoyancy gradients from

450 monthly 5 m temperature and salinity (0.5° resolution), and then infer approximate monthly values
451 of A_v using the surface boundary condition, $\rho A_v = \tau_w (\partial u / \partial z)^{-1}$, with the near-surface shear mag-
452 nitude approximated using CFSR velocities at 5 and 15 m, $\partial u / \partial z \sim |\mathbf{u}(-5) - \mathbf{u}(-15)| / 10$. Alter-
453 nate parameterizations of A_v were tested, including wind-stress only parameterizations (Wenegrat
454 et al. 2014) and bulk Richardson number closures (Pollard et al. 1973), and found to give sim-
455 ilar results (not shown here). Monthly values of the Stokes transport and τ_{geo} over the period
456 2001-2011 are then used to form climatologies of γ_{GEO} and γ_{CS} .

457 Figures 9 and 10 show the global seasonal climatology of γ_{GEO} and γ_{CS} , respectively. The depen-
458 dence on latitude through the Coriolis frequency is apparent in both quantities, with γ_{GEO} peaking
459 at low latitudes, and γ_{CS} dominating at higher latitudes (figure 11). Regional variability is also
460 evident, with γ_{GEO} enhanced in boundary currents, along the equatorward edges of the subtropical
461 gyres, and through much of the Indian ocean and eastern subtropical Pacific. These parameterized
462 results can be compared to estimates derived from model output and alternate parameterizations
463 of A_v , which indicate similar spatial patterns (Chu 2015; Cronin and Tozuka 2015).

464 In the zonal average, and temporal average, γ_{CS} becomes larger than γ_{GEO} poleward of 15°
465 (figures 10 and 11), following a spatial pattern that in large part reflects the variability in Stokes
466 transport (McWilliams and Restrepo 1999). This latitudinal pattern may also reflect the effect
467 of the coarse resolution products utilized here on estimating γ_{GEO} , as the first baroclinic Rossby
468 radius at 15° is ~ 100 km (Chelton et al. 1998), which is close to the resolved meridional Nyquist
469 wavelength, and hence ∇b may be underestimated at higher latitudes. Wide swaths of the world
470 oceans have $\gamma_{CS} \sim 0.25$, emphasizing how important these effects may be for Ekman layer currents.
471 Intensification of γ_{CS} in the southern ocean is also evident. In the Northern Hemisphere there is
472 a general enhancement of γ_{CS} in the eastern side of the ocean basins, with seasonal variability in

473 both extent and magnitude, resulting from enhanced Stokes transport associated with increased
474 wintertime wind-forcing.

475 The relative influences of the geostrophic stress and the Coriolis-Stokes stress can be consid-
476 ered using the joint probability density function (PDF) of the monthly estimates of γ_{GEO} and γ_{CS} ,
477 evaluated between $5^\circ - 73.5^\circ$ from 2001-2011 (figure 12). Consistent with the spatial maps, the
478 PDF has a broad peak at $\gamma_{CS} \sim 0.1 - 0.25$ with negligible γ_{GEO} . However, the distribution of γ_{GEO}
479 is long-tailed, reflecting its spatial and temporal inhomogeneity, evident in comparing an example
480 month (figure 13) and the climatological maps (figure 9). Considering the total relative change in
481 the effective surface stress arising from both the geostrophic stress and the Coriolis-Stokes stress,
482 $\gamma_T = \gamma_{GEO} + \gamma_{CS}$, 36% of all points have $\gamma_T > 0.25$. Together the estimates presented above, while
483 only a rough approximation, suggest that surface waves will be of $O(1)$ importance for much
484 of the extra-tropics, while baroclinic pressure gradients will dominate at low latitudes, in frontal
485 systems, and potentially over shorter timescales, and smaller spatial scales, than resolved here,
486 specifically at the submesoscale, where geostrophic stress effects have been demonstrated to sig-
487 nificantly modify the ageostrophic flow (Ponte et al. 2013; Gula et al. 2014; McWilliams et al.
488 2015).

489 *b. Horizontal Fluxes*

490 The proceeding analysis, and theory, highlights how ocean sources of stress can be expected to
491 modify the frictional response within the near-surface layer, effecting the magnitude, direction, and
492 vertical profile of the ageostrophic flow. These modifications to the ageostrophic velocity can often
493 be approximated using the concept of an effective stress, τ_{Eff} (section 3), leading to a modified
494 Ekman velocity scale of, $u_{Ek} \sim \tau_{Eff}/(\rho f h_{Ek})$. This has wide-ranging implications for horizontal
495 advective fluxes, where for example, the geostrophic stress will always enhance heat flux down

496 the buoyancy gradient relative to the classic Ekman solution, as well as for other dynamically
 497 important quantities such as the wind-work on the total ageostrophic flow, $\tau_w \cdot \mathbf{u}_{Ek}$, which will be
 498 reduced for winds aligned with the surface frontal jet (down-front winds), and enhanced for winds
 499 aligned against the frontal jet (up-front winds).

500 A brief example, which highlights the role of vertical structure in A_v , is given by considering
 501 the differential horizontal buoyancy flux across the surface Ekman layer, which can change the
 502 stratification, and hence the potential vorticity (PV), of the near surface layer (Thomas and Ferrari
 503 2008). A scaling for the frictional flux of the vertical component of PV due to a surface wind
 504 stress in the presence of a horizontal buoyancy gradient is given by (Thomas 2005; Thomas and
 505 Ferrari 2008),

$$J_z^F \sim \frac{\tau_w}{\rho h_{Ek}} \nabla b. \quad (29)$$

506 However, if A_v is allowed to vary vertically, with depth scale h_{Av} , this scaling is modified to
 507 become,

$$J_z^F \sim \frac{\tau_w}{\rho h_{Ek}} \nabla b \left(1 + \frac{h_{Ek}}{4h_{Av}} \right). \quad (30)$$

508 This relationship is shown in figure 14, for a wind stress aligned with the front, and an expo-
 509 nential A_v profile that decreases (increases), $h_{Av} > 0$ ($h_{Av} < 0$), with depth. As $|h_{Av}|$ approaches
 510 h_{Ek} the surface cross-front current is enhanced (reduced) for $h_{Av} > 0$ ($h_{Av} < 0$), modifying the fric-
 511 tional PV flux. A similar result can be easily derived for the influence of vertical structure of A_v
 512 on the frictional PV flux associated with the frontal spin down by the geostrophic stress (Thomas
 513 and Ferrari 2008). Thus, the vertical structure of mixing is linked to the flux of vertical potential
 514 vorticity through its effect on the differential horizontal advection of buoyancy.

515 A conceptual example of how this might affect the ocean boundary layer is found by con-
 516 sidering the near-surface response to up-front and down-front winds. Down-front winds advect

517 dense water over light water, leading to gravitational instability, whereas up-front winds advect
518 light water over dense, enhancing stratification (Thomas and Lee 2005). Making the idealization
519 that down-front winds lead to a well-mixed layer with $A_v \sim \text{constant}$, whereas up-front winds lead
520 to a stratified near-surface layer with A_v decreasing with depth, would imply the existence of an
521 asymmetry in PV fluxes between the two cases. Consequently, for the same wind stress and buoy-
522 ancy gradient magnitudes, wind-driven frictional PV fluxes may be enhanced in up-front wind
523 conditions relative to down-front winds, providing a possible alternative route to the creation of
524 positively skewed PV distributions (Thomas 2007).

525 **6. Summary**

526 In this manuscript we present an approximate solution to the generalized Ekman (Cronin and
527 Kessler 2009), or Turbulent Thermal Wind (Gula et al. 2014; McWilliams et al. 2015), balance.
528 While this theory omits many aspects of boundary layer physics that are likely to be active in the
529 real ocean, the simplicity and generality of the solution provides a useful tool for gaining insight
530 into the underlying dynamics beyond that available from numerical methods. The full solution,
531 (7), given in terms of an integral over a Green's function, can be applied quite generally to a variety
532 of sources of near-surface shear, and further allows for arbitrary vertical structure in A_v , subject to
533 the constraints imposed by the WKB method. Many existing modified Ekman theories can thus be
534 considered as particular cases of this solution, providing a framework for comparing their effects
535 on ageostrophic ocean currents.

536 Two important aspects of surface layer dynamics which are not as readily accommodated in this
537 framework are time-dependence, and non-linearity. Observations suggest significant diurnal vari-
538 atiability of near-surface shear (Price et al. 1986; Schudlich and Price 1998; Cronin and Kessler
539 2009; Smyth et al. 2013; Wenegrat and McPhaden 2015), which has been suggested as an expla-

540 nation of observed discrepancies with classic Ekman theory (Price and Sundermeyer 1999). How-
541 ever, analysis of near-surface velocity observations appears to suggest that some of the observed
542 features which have been used to argue for the role of time-variability, such as a flattened spiral, can
543 also be very well explained by alternate mechanisms that do not invoke time-dependence (Lewis
544 and Belcher 2004; Polton et al. 2005; Cronin and Kessler 2009). Disentangling these effects using
545 observations is further complicated by measurement challenges, particularly for moored observa-
546 tions which can be biased by surface waves (Rascle and Arduin 2009). A focus of future work
547 should be clarifying the relative contributions of, and interactions between, the diverse sources of
548 near-surface ageostrophic flow.

549 Non-linear effects may be of particular importance in examining sharp horizontal buoyancy
550 gradients (Stern 1965; Niiler 1969; Thomas and Rhines 2002; Mahadevan and Tandon 2006).
551 However, a range of modeling efforts which include more complete physics indicate that the basic
552 dynamical mechanisms discussed here continue to be of first order importance in the boundary
553 layer, even at high ε (Thompson 2000; Nagai et al. 2006; Ponte et al. 2013; Gula et al. 2014;
554 McWilliams et al. 2015). We also note that the work of Wu and Blumen (1982), and (Tan 2001),
555 can be considered as a blueprint for how the semi-geostrophic momentum approximation could be
556 incorporated into the solution given here.

557 Examining two limiting cases, the first for Stokes shear of shallow depth relative to h_{Ek} , and
558 the second for a front much deeper than h_{Ek} , reveals the key underlying dynamics. Ocean sources
559 of shear, in the presence of viscosity, act as sources of stress. These ocean sources of stress
560 are, as a first approximation, independent of the surface wind stress, and are capable of driving
561 their own ageostrophic flow, including creating a surface Ekman layer. The equivalency of the
562 closed form solutions for the two limiting cases emphasizes how robust this interpretation of the
563 underlying dynamics is, suggesting the same interpretation holds for the more general Green's

564 function solution (7), and highlighting a previously unnoted connection between the frictional
565 effects of surface waves and fronts.

566 The solutions presented here are unique in their ability to incorporate arbitrary vertical structure
567 in A_v , which is motivated physically by modeling and direct turbulence measurements (Zikanov
568 et al. 2003; Kirincich 2013; Soloviev and Lukas 2014), and is shown here to lead to modifications
569 of both horizontal and vertical flows. Improved understanding of the spatial variability of mixing
570 is key to understanding and parameterizing these effects on boundary layer flow. Finally, it should
571 be emphasized that the various dynamical processes discussed here should not be considered as
572 the addition of new parameters to the Ekman problem, but rather as fundamental components of
573 the frictional response of the ocean boundary layer whose influence may be of the same order
574 of magnitude as the surface wind stress throughout large portions of the global oceans. The total
575 frictional ageostrophic response is a combination of a response to the surface wind, as in the classic
576 Ekman theory, and a response to ocean sources of shear.

577 *Acknowledgments.* We would like to thank Leah Johnson, Hayley Dossier, and Andrew Shao for
578 many helpful discussions during the course of this work. The comments and suggestions of two
579 anonymous reviewers improved this manuscript. This publication is partially funded by the Joint
580 Institute for the Study of the Atmosphere and Ocean (JISAO) under NOAA Cooperative Agree-
581 ment NA10OAR4320148, Contribution No. 2465. PMEL contribution number 4384. WaveWatch
582 III model output is available from the IOWAGA group at: <http://wwz.ifremer.fr/iowaga/Products>.
583 NCEP CFSR data is available at: <http://rda.ucar.edu/pub/cfsr.html>.

584 APPENDIX A

585 Derivation

586 Let $A_v(z) = A_{v0}\psi(z)$, then, after non-dimensionalizing (3) as discussed in section (2), we have,

$$Ek\tau'' - \frac{i}{\psi(z)}\tau = \xi(z), \quad (A1)$$

587

$$\tau(h) = \tau_w, \quad (A2)$$

588

$$\tau(0) = 0, \quad (A3)$$

589 where primes indicate vertical derivatives and all variables are non-dimensional unless otherwise
 590 noted. The RHS of (A1) is given in terms of a generic inhomogeneous forcing function, $\xi(z)$,
 591 which could arise from geostrophic shear or Coriolis-Stokes shear as discussed in section 3. Solv-
 592 ing first for the homogenous solution, and making the WKB assumption,

$$\tau \propto e^{(S_0+S_1\delta+S_2\delta^2+\dots)/\delta}, \quad (A4)$$

593 gives,

$$Ek \left[\frac{S_0''}{\delta} + \frac{S_0'^2}{\delta^2} + \frac{2S_0'S_1'}{\delta} + S_1'' + S_1'^2 \right] \tau - \frac{i}{\psi(z)}\tau = 0. \quad (A5)$$

594 The distinguished limit for the parameter δ is therefore, $\delta \sim Ek^{\frac{1}{2}}$, and the balance conditions
 595 are given by,

$$O(\delta^{-2}): S_0' = \pm \sqrt{\frac{i}{\psi(z)}}, \quad (A6)$$

596

$$O(\delta^{-1}): S_1' = -\frac{S_0''}{2S_0'}. \quad (A7)$$

597 Taking the positive root of S_0' gives,

$$S_0 = \sqrt{i} \int_{-h}^z \psi(Z)^{-\frac{1}{2}} dZ, \quad (A8)$$

598 and,

$$S_1 = \frac{1}{4} \log \psi(z). \quad (A9)$$

599 A similar argument is followed for the negative root, giving the two solutions to the ODE, which
600 dimensionally are given by,

$$\tau(z) = C_1 A_v(z)^{\frac{1}{4}} e^{\theta(z)} + C_2 A_v(z)^{\frac{1}{4}} e^{-\theta(z)}, \quad (\text{A10})$$

601 where,

$$\theta(z) = \sqrt{if} \int_{-h}^z A_v(Z)^{-\frac{1}{2}} dZ. \quad (\text{A11})$$

602 For the WKB approximation to hold, two conditions must be satisfied (Bender and Orszag
603 1978),

$$\frac{Ek^{\frac{1}{2}} S_1}{S_0} \ll 1, \quad Ek^{\frac{1}{2}} \rightarrow 0, \quad (\text{A12})$$

604

$$Ek^{\frac{1}{2}} S_2 \ll 1, \quad Ek^{\frac{1}{2}} \rightarrow 0, \quad (\text{A13})$$

605 discussed further in Appendix B.

606 Variation of parameters gives the inhomogeneous portion of the solution,

$$\tau_p = -y_1 \int \frac{y_2 \xi(z)}{W(y_1, y_2)} dz + y_2 \int \frac{y_1 \xi(z)}{W(y_1, y_2)} dz. \quad (\text{A14})$$

607 Where W is the Wronskian,

$$W(y_1, y_2) = y_1 y_2' - y_2 y_1' = -2\sqrt{if}. \quad (\text{A15})$$

608 Thus,

$$\tau_p = A_v(z)^{\frac{1}{4}} e^{\theta(z)} \int \frac{e^{-\theta(z)} A_v(z)^{\frac{1}{4}} \xi(z)}{2\sqrt{if}} dz - A_v(z)^{\frac{1}{4}} e^{-\theta(z)} \int \frac{e^{\theta(z)} A_v(z)^{\frac{1}{4}} \xi(z)}{2\sqrt{if}} dz. \quad (\text{A16})$$

609 Changing the limits of integration gives,

$$\tau_p = \int_0^z \frac{\sinh[\theta(z) - \theta(s)] A_v(z)^{\frac{1}{4}} A_v(s)^{\frac{1}{4}} \xi(s)}{\sqrt{if}} ds. \quad (\text{A17})$$

610 So, the total solution, before application of the boundary conditions, is given by,

$$\tau_t(z) = C_1 A_v(z)^{\frac{1}{4}} e^{\theta(z)} + C_2 A_v(z)^{\frac{1}{4}} e^{-\theta(z)} + \int_0^z \frac{\sinh[\theta(z) - \theta(s)] A_v(z)^{\frac{1}{4}} A_v(s)^{\frac{1}{4}} \xi(s)}{\sqrt{if}} ds. \quad (\text{A18})$$

611 Applying the surface BC gives,

$$\tau_w = C_1 A_v(0)^{\frac{1}{4}} e^{\theta(0)} + C_2 A_v(0)^{\frac{1}{4}} e^{-\theta(0)}, \quad (\text{A19})$$

612 therefore,

$$\begin{aligned} \tau_t(z) = & 2C_1 A_v(z)^{\frac{1}{4}} e^{\theta(0)} \sinh[\theta(z) - \theta(0)] + \tau_w \left(\frac{A_v(z)}{A_v(0)} \right)^{\frac{1}{4}} e^{\theta(0) - \theta(z)} \\ & + \int_0^z \frac{\sinh[\theta(z) - \theta(s)] A_v(z)^{\frac{1}{4}} A_v(s)^{\frac{1}{4}} \xi(s)}{\sqrt{if}} ds. \end{aligned} \quad (\text{A20})$$

613 The lower BC gives,

$$\begin{aligned} 0 = & 2C_1 A_v(-h)^{\frac{1}{4}} e^{\theta(0)} \sinh[\theta(-h) - \theta(0)] + \tau_w \left(\frac{A_v(-h)}{A_v(0)} \right)^{\frac{1}{4}} e^{\theta(0) - \theta(-h)} \\ & + \int_0^{-h} \frac{\sinh[\theta(-h) - \theta(s)] A_v(-h)^{\frac{1}{4}} A_v(s)^{\frac{1}{4}} \xi(s)}{\sqrt{if}} ds. \end{aligned} \quad (\text{A21})$$

614 Following Hidaka (1955), we multiply equation (A20) by $\sinh[-\theta(0)]$, equation (A21) by
615 $-\left(\frac{A_v(z)}{A_v(-h)}\right)^{\frac{1}{4}} \sinh[\theta(z) - \theta(0)]$, and add them, giving,

$$\begin{aligned} \tau(z) = & \tau_w \left(\frac{A_v(z)}{A_v(0)} \right)^{\frac{1}{4}} \frac{\sinh[\theta(z)]}{\sinh[\theta(0)]} + \int_0^z \frac{\sinh[\theta(z) - \theta(s)] \sinh[\theta(0)] \xi(s) A_v(s)^{\frac{1}{4}} A_v(z)^{\frac{1}{4}}}{(if)^{\frac{1}{2}} \sinh[\theta(0)]} ds \\ & - \int_0^{-h} \frac{\sinh[\theta(z) - \theta(0)] \sinh[\theta(s)] \xi(s) A_v(s)^{\frac{1}{4}} A_v(z)^{\frac{1}{4}}}{(if)^{\frac{1}{2}} \sinh[\theta(0)]} ds. \end{aligned} \quad (\text{A22})$$

616 This can be re-written as,

$$\tau(z) = \tau_w \left(\frac{A_v(z)}{A_v(0)} \right)^{\frac{1}{4}} \frac{\sinh[\theta(z)]}{\sinh[\theta(0)]} + \int_{-h}^0 G(z, s) \xi(s) ds, \quad (\text{A23})$$

617

$$\theta(z) = \sqrt{if} \int_{-h}^z A_v(Z)^{-\frac{1}{2}} dZ, \quad (\text{A24})$$

618

$$G(z, s) = \begin{cases} \frac{\sinh[\theta(z)] \sinh[\theta(s) - \theta(0)] A_v(s)^{\frac{1}{4}} A_v(z)^{\frac{1}{4}}}{\sinh[\theta(0)] \sqrt{if}} & \text{if } s > z \\ \frac{\sinh[\theta(s)] \sinh[\theta(z) - \theta(0)] A_v(s)^{\frac{1}{4}} A_v(z)^{\frac{1}{4}}}{\sinh[\theta(0)] \sqrt{if}} & \text{if } s < z. \end{cases} \quad (\text{A25})$$

Accuracy of approximate solution

The validity of the physical-optics WKB approximation requires the criteria (A12) and (A13) be satisfied (Bender and Orszag 1978). The relative error in the approximation will then be a function of the small parameter $\delta \sim Ek^{1/2}$ and the first ignored term, S_2 , in (A4), which involves both first and second derivatives of A_v . Thus, errors will be a function of the Ekman number, Ek , as well as the particular vertical structure of A_v . Anecdotally, the WKB solution (7) has proven extremely accurate across a wide-range of vertical structures of A_v , and values of Ek , considered in developing the model (see also Grisogono 1995; Berger and Grisogono 1998). However, to better illustrate the accuracy of the approximate solution we consider the relative error associated with 3 idealized forms of A_v (figure B1).

Case I is a simple exponentially decaying profile,

$$A_v(z) = A_{v0} e^{-\frac{\hat{z}}{0.125}}, \quad (\text{B1})$$

chosen for its analytic simplicity, and consistency with observations (Peters et al. 1988; Dillon et al. 1989). Case II is a linearly decaying profile,

$$A_v(z) = A_{v0} \left(1 + \frac{\hat{z}}{1 + \mu} \right), \quad (\text{B2})$$

where μ is a small value added to avoid a singularity at $z = -h$. Case III is a modified Gaussian profile (Parmhed et al. 2005),

$$A_v(z) = A_{v0} \phi \hat{z} e^{-\frac{1}{2} \left(\frac{\hat{z}}{0.25} \right)^2} \quad (\text{B3})$$

where, $\phi = e^{1/2}/0.25$, which approximates the polynomial profile of O'Brien (1970). This profile violates (A12) in a thin layer near $z = 0$, where $A_v \rightarrow 0$, and hence we evaluate the error associated

637 with this profile only over the depth range where the WKB solution can be expected to be valid.
 638 Namely $\hat{z} \leq z_p$, where z_p is given by Parmhed et al. (2005) as,

$$z_p = -\frac{1}{4} \left[W \left(\frac{2}{\sqrt{\phi}} \right) \right]^2, \quad (\text{B4})$$

639 where W is the Lambert W function (Corless et al. 1996). For the values used here, $z_p = -0.06$,
 640 thus, rather than patching an additional inner solution for $\hat{z} > z_p$, we make the simplifying approx-
 641 imation of applying the surface boundary condition directly to the WKB solution at z_p , similar to
 642 the introduction of a roughness length scale (Madsen 1977), and equivalent in the error analysis to
 643 the requirement that any inner solution be exact.

644 To form an estimate of the relative error as a function of Ek , WKB solutions (7) are compared to
 645 numeric solutions, found using a shooting method, and the normalized maximum error identified
 646 in each vertical profile,

$$\widehat{\tau}_{err}(Ek) = \frac{\max\{|\tau_{WKB}(z, Ek) - \tau_{num}(z, Ek)|\}}{\max\{|\tau_{num}(z, Ek)|\}}. \quad (\text{B5})$$

647 Results are plotted in figure B2, for wind stress only forcing (top), and solutions forced by a
 648 vertically uniform buoyancy gradient (bottom). Also plotted for reference is the value of the small
 649 parameter, $\delta \sim Ek^{1/2}$. Errors are generally small, and, for $Ek \leq 10^{-1}$, the only case with relative
 650 errors exceeding 10% is the modified exponential profile, (B3). The errors associated with this
 651 profile are strongly dependent on the choice of patching depth, z_p , rather than the overall vertical
 652 structure, as can be anticipated through the logarithmic singularity evident in (A12). Hence caution
 653 is required in applying (7) in cases where $A_v \rightarrow 0$ near a boundary. Despite the limitations of the
 654 WKB method, its simplicity, and generality, argue its utility, particularly in comparison to the
 655 often strict parameter requirements associated with other analytic solutions techniques.

656 References

- 657 Aiki, H., and R. J. Greatbatch, 2012: Thickness-Weighted Mean Theory for the Effect of Sur-
658 face Gravity Waves on Mean Flows in the Upper Ocean. *Journal of Physical Oceanogra-*
659 *phy*, **42** (5), 725–747, doi:10.1175/JPO-D-11-095.1, URL [http://journals.ametsoc.org/doi/abs/](http://journals.ametsoc.org/doi/abs/10.1175/JPO-D-11-095.1)
660 [10.1175/JPO-D-11-095.1](http://journals.ametsoc.org/doi/abs/10.1175/JPO-D-11-095.1).
- 661 Belcher, S. E., and Coauthors, 2012: A global perspective on Langmuir turbulence in the ocean
662 surface boundary layer: FRONTIER. *Geophysical Research Letters*, **39** (18), n/a–n/a, doi:10.
663 1029/2012GL052932, URL <http://doi.wiley.com/10.1029/2012GL052932>.
- 664 Bender, C. M., and S. A. Orszag, 1978: *Advanced mathematical methods for scientists and engi-*
665 *neers*. Springer, New York.
- 666 Berger, B. W., and B. Grisogono, 1998: The baroclinic, variable eddy viscosity Ekman layer.
667 *Boundary-Layer Meteorology*, **87** (3), 363–380, URL [http://link.springer.com/article/10.1023/](http://link.springer.com/article/10.1023/A:1001076030166)
668 [A:1001076030166](http://link.springer.com/article/10.1023/A:1001076030166).
- 669 Boccaletti, G., R. Ferrari, and B. Fox-Kemper, 2007: Mixed Layer Instabilities and Restratifi-
670 cation. *Journal of Physical Oceanography*, **37** (9), 2228–2250, doi:10.1175/JPO3101.1, URL
671 <http://journals.ametsoc.org/doi/abs/10.1175/JPO3101.1>.
- 672 Bonjean, F., and G. S. E. Lagerloef, 2002: Diagnostic Model and Analysis of the Surface Currents
673 in the Tropical Pacific Ocean. *Journal of Physical Oceanography*, **32** (10), 2938–2954, doi:
674 10.1175/1520-0485(2002)032<2938:DMAAOT>2.0.CO;2.
- 675 Buckingham, E., 1914: On Physically Similar Systems; Illustrations of the Use of Dimensional
676 Equations. *Physical Review*, **4** (4), 345–376, doi:10.1103/PhysRev.4.345, URL [http://link.aps.](http://link.aps.org/doi/10.1103/PhysRev.4.345)
677 [org/doi/10.1103/PhysRev.4.345](http://link.aps.org/doi/10.1103/PhysRev.4.345).

678 Caldwell, D. R., C. W. Van Atta, and K. N. Helland, 1972: A laboratory study of the turbulent
679 Ekman layer. *Geophysical Fluid Dynamics*, **3** (1), 125–160, doi:10.1080/03091927208236078,
680 URL <http://www.tandfonline.com/doi/abs/10.1080/03091927208236078>.

681 Chelton, D. B., R. A. deSzoeke, M. G. Schlax, K. El Naggar, and N. Siwertz, 1998: Geograph-
682 ical Variability of the First Baroclinic Rossby Radius of Deformation. *Journal of Physical*
683 *Oceanography*, **28** (3), 433–460, doi:10.1175/1520-0485(1998)028<0433:GVOTFB>2.0.CO;
684 2, URL <http://journals.ametsoc.org/doi/abs/10.1175/1520-0485%281998%29028%3C0433%3AGVOTFB%3E2.0.CO%3B2>.

686 Chereskin, T. K., 1995: Direct evidence for an Ekman balance in the California Current. *Journal of*
687 *Geophysical Research*, **100** (C9), 18 261, doi:10.1029/95JC02182, URL <http://doi.wiley.com/10.1029/95JC02182>.

689 Chereskin, T. K., and D. Roemmich, 1991: A Comparison of Measured and Wind-derived Ekman
690 Transport at 11N in the Atlantic Ocean. *Journal of Physical Oceanography*, **21** (6), 869–878,
691 doi:10.1175/1520-0485(1991)021<0869:ACOMAW>2.0.CO;2, URL <http://journals.ametsoc.org/doi/abs/10.1175/1520-0485%281991%29021%3C0869%3AACOMAW%3E2.0.CO%3B2>.

693 Chu, P. C., 2015: Ekman Spiral in a Horizontally Inhomogeneous Ocean with Varying Eddy
694 Viscosity. *Pure and Applied Geophysics*, doi:10.1007/s00024-015-1063-4, URL <http://link.springer.com/10.1007/s00024-015-1063-4>.

696 Corless, R. M., G. H. Gonnet, D. E. G. Hare, D. J. Jeffrey, and D. E. Knuth, 1996: On the
697 Lambert W function. *Advances in Computational Mathematics*, **5** (1), 329–359, doi:10.1007/
698 BF02124750, URL <http://link.springer.com/10.1007/BF02124750>.

699 Cronin, M. F., and W. S. Kessler, 2009: Near-Surface Shear Flow in the Tropical Pacific
700 Cold Tongue Front*. *Journal of Physical Oceanography*, **39** (5), 1200–1215, doi:10.1175/
701 2008JPO4064.1, URL <http://journals.ametsoc.org/doi/abs/10.1175/2008JPO4064.1>.

702 Cronin, M. F., and T. Tozuka, 2015: Ekman ocean response to wind forcing in extratropical frontal
703 regions, Phoenix, AZ. URL [https://ams.confex.com/ams/95Annual/webprogram/Paper267544.](https://ams.confex.com/ams/95Annual/webprogram/Paper267544.html)
704 [html](https://ams.confex.com/ams/95Annual/webprogram/Paper267544.html).

705 Csanady, G., 1982: Frictional Secondary Circulation Near An Upwelled Thermocline. Woods
706 Hole Oceanog. Inst. Tech. Rept. WHOI-82-52.

707 Dewey, R. K., and J. N. Moum, 1990: Enhancement of fronts by vertical mixing. *Journal of*
708 *Geophysical Research*, **95** (C6), 9433, doi:10.1029/JC095iC06p09433, URL [http://doi.wiley.](http://doi.wiley.com/10.1029/JC095iC06p09433)
709 [com/10.1029/JC095iC06p09433](http://doi.wiley.com/10.1029/JC095iC06p09433).

710 Dillon, T. M., J. N. Moum, T. K. Chereskin, and D. R. Caldwell, 1989: Zonal Momen-
711 tum Balance at the Equator. *Journal of Physical Oceanography*, **19** (5), 561–570, doi:
712 10.1175/1520-0485(1989)019<0561:ZMBATE>2.0.CO;2, URL [http://journals.ametsoc.org/doi/](http://journals.ametsoc.org/doi/abs/10.1175/1520-0485%281989%29019%3C0561%3AZMBATE%3E2.0.CO%3B2)
713 [abs/10.1175/1520-0485%281989%29019%3C0561%3AZMBATE%3E2.0.CO%3B2](http://journals.ametsoc.org/doi/abs/10.1175/1520-0485%281989%29019%3C0561%3AZMBATE%3E2.0.CO%3B2).

714 Ekman, V., 1905: On the influence of the earth's rotation on ocean currents. *Ark. Mat. Astron.*
715 *Fys.*, **2**, 1–53.

716 Elipot, S., and S. T. Gille, 2009: Ekman layers in the Southern Ocean: spectral models and ob-
717 servations, vertical viscosity and boundary layer depth. *Ocean Science*, **5** (2), 115–139, doi:
718 10.5194/os-5-115-2009, URL <http://www.ocean-sci.net/5/115/2009/>.

719 Garrett, C. J. R., and J. W. Loder, 1981: Dynamical Aspects of Shallow Sea Fronts. *Philosophical*
720 *Transactions of the Royal Society A: Mathematical, Physical and Engineering Sciences*,

721 **302 (1472)**, 563–581, doi:10.1098/rsta.1981.0183, URL <http://rsta.royalsocietypublishing.org/>
722 [cgi/doi/10.1098/rsta.1981.0183](http://rsta.royalsocietypublishing.org/cgi/doi/10.1098/rsta.1981.0183).

723 Gill, A. E., 1982: *Atmosphere-ocean dynamics*. International geophysics series, Academic Press,
724 New York.

725 Grant, A. L. M., and S. E. Belcher, 2009: Characteristics of Langmuir Turbulence in the
726 Ocean Mixed Layer. *Journal of Physical Oceanography*, **39 (8)**, 1871–1887, doi:10.1175/
727 2009JPO4119.1, URL <http://journals.ametsoc.org/doi/abs/10.1175/2009JPO4119.1>.

728 Grisogono, B., 1995: A generalized Ekman layer profile with gradually varying eddy diffusivities.
729 *Quarterly Journal of the Royal Meteorological Society*, **121 (522)**, 445–453, doi:10.1002/qj.
730 49712152211, URL <http://doi.wiley.com/10.1002/qj.49712152211>.

731 Gula, J., M. J. Molemaker, and J. C. McWilliams, 2014: Submesoscale Cold Filaments in the Gulf
732 Stream. *Journal of Physical Oceanography*, **44 (10)**, 2617–2643, doi:10.1175/JPO-D-14-0029.
733 1, URL <http://journals.ametsoc.org/doi/abs/10.1175/JPO-D-14-0029.1>.

734 Hidaka, K., 1955: Wind circulation in a two-layer zonal ocean. *Jap. J. Geophys*, **1**.

735 Huang, N. E., 1971: Derivation of Stokes drift for a deep-water random gravity wave field.
736 *Deep Sea Research and Oceanographic Abstracts*, **18 (2)**, 255–259, doi:10.1016/0011-7471(71)
737 90115-X, URL <http://linkinghub.elsevier.com/retrieve/pii/001174717190115X>.

738 Huang, N. E., 1979: On surface drift currents in the ocean. *Journal of Fluid Mechanics*, **91 (01)**,
739 191, doi:10.1017/S0022112079000112.

740 Jenkins, A. D., 1986: A Theory for Steady and Variable Wind-and Wave-Induced Cur-
741 rents. *Journal of Physical Oceanography*, **16 (8)**, 1370–1377, doi:10.1175/1520-0485(1986)

742 016<1370:ATFSAV>2.0.CO;2, URL [http://journals.ametsoc.org/doi/abs/10.1175/1520-0485%](http://journals.ametsoc.org/doi/abs/10.1175/1520-0485%281986%29016%3C1370%3AATFSAV%3E2.0.CO%3B2)
743 [281986%29016%3C1370%3AATFSAV%3E2.0.CO%3B2](http://journals.ametsoc.org/doi/abs/10.1175/1520-0485%281986%29016%3C1370%3AATFSAV%3E2.0.CO%3B2).

744 Kirincich, A. R., 2013: Long-Term Observations of Turbulent Reynolds Stresses over the In-
745 ner Continental Shelf. *Journal of Physical Oceanography*, **43** (12), 2752–2771, doi:10.1175/
746 JPO-D-12-0153.1, URL <http://journals.ametsoc.org/doi/abs/10.1175/JPO-D-12-0153.1>.

747 Komen, G. J., Ed., 1996: *Dynamics and modelling of ocean waves*. 1st ed., Cambridge Univ. Press,
748 Cambridge.

749 Large, W. G., J. C. McWilliams, and S. C. Doney, 1994: Oceanic vertical mixing: A review and
750 a model with a nonlocal boundary layer parameterization. *Reviews of Geophysics*, **32** (4), 363,
751 doi:10.1029/94RG01872, URL <http://doi.wiley.com/10.1029/94RG01872>.

752 Lewis, D., and S. Belcher, 2004: Time-dependent, coupled, Ekman boundary layer solutions in-
753 corporating Stokes drift. *Dynamics of Atmospheres and Oceans*, **37** (4), 313–351, doi:10.1016/j.
754 dynatmoce.2003.11.001, URL <http://linkinghub.elsevier.com/retrieve/pii/S0377026503000605>.

755 Lupini, R., A. Speranza, and A. Trevisan, 1975: A re-examination of the classical formulation
756 of turbulent Ekman boundary layer flow. *Il Nuovo Cimento B Series 11*, **25** (2), 871–881, doi:
757 10.1007/BF02724758, URL <http://link.springer.com/10.1007/BF02724758>.

758 Madsen, O. S., 1977: A Realistic Model of the Wind-Induced Ekman Boundary Layer.
759 *Journal of Physical Oceanography*, **7** (2), 248–255, doi:10.1175/1520-0485(1977)007<0248:
760 ARMOTW>2.0.CO;2, URL [http://journals.ametsoc.org/doi/abs/10.1175/1520-0485%](http://journals.ametsoc.org/doi/abs/10.1175/1520-0485%281977%29007%3C0248%3AARMOTW%3E2.0.CO%3B2)
761 [281977%](http://journals.ametsoc.org/doi/abs/10.1175/1520-0485%281977%29007%3C0248%3AARMOTW%3E2.0.CO%3B2)
[29007%3C0248%3AARMOTW%3E2.0.CO%3B2](http://journals.ametsoc.org/doi/abs/10.1175/1520-0485%281977%29007%3C0248%3AARMOTW%3E2.0.CO%3B2).

- 762 Mahadevan, A., and A. Tandon, 2006: An analysis of mechanisms for submesoscale vertical
763 motion at ocean fronts. *Ocean Modelling*, **14** (3-4), 241–256, doi:10.1016/j.ocemod.2006.05.
764 006, URL <http://linkinghub.elsevier.com/retrieve/pii/S1463500306000540>.
- 765 McPhaden, M. J., 1981: Continuously Stratified Models of the Steady-State Equatorial Ocean.
766 *Journal of Physical Oceanography*, **11** (3), 337–354, doi:10.1175/1520-0485(1981)011<0337:
767 CSMOTS>2.0.CO;2, URL [http://journals.ametsoc.org/doi/abs/10.1175/1520-0485%281981%](http://journals.ametsoc.org/doi/abs/10.1175/1520-0485%281981%29011%3C0337%3ACSMOTS%3E2.0.CO%3B2)
768 [29011%3C0337%3ACSMOTS%3E2.0.CO%3B2](http://journals.ametsoc.org/doi/abs/10.1175/1520-0485%281981%29011%3C0337%3ACSMOTS%3E2.0.CO%3B2).
- 769 McWilliams, J. C., and B. Fox-Kemper, 2013: Oceanic wave-balanced surface fronts and fil-
770 aments. *Journal of Fluid Mechanics*, **730**, 464–490, doi:10.1017/jfm.2013.348, URL [http://](http://www.journals.cambridge.org/abstract_S0022112013003480)
771 www.journals.cambridge.org/abstract_S0022112013003480.
- 772 McWilliams, J. C., J. Gula, M. J. Molemaker, L. Renault, and A. F. Shchepetkin, 2015: Filament
773 Frontogenesis by Boundary Layer Turbulence. *Journal of Physical Oceanography*, doi:10.1175/
774 JPO-D-14-0211.1, URL <http://journals.ametsoc.org/doi/abs/10.1175/JPO-D-14-0211.1>.
- 775 McWilliams, J. C., E. Huckle, J. Liang, and P. P. Sullivan, 2014: Langmuir Turbulence in Swell.
776 *Journal of Physical Oceanography*, **44** (3), 870–890, doi:10.1175/JPO-D-13-0122.1, URL [http://](http://journals.ametsoc.org/doi/abs/10.1175/JPO-D-13-0122.1)
777 journals.ametsoc.org/doi/abs/10.1175/JPO-D-13-0122.1.
- 778 McWilliams, J. C., E. Huckle, J.-H. Liang, and P. P. Sullivan, 2012: The Wavy Ekman Layer:
779 Langmuir Circulations, Breaking Waves, and Reynolds Stress. *Journal of Physical Oceanogra-*
780 *phy*, **42** (11), 1793–1816, doi:10.1175/JPO-D-12-07.1.
- 781 McWilliams, J. C., E. Huckle, and A. F. Shchepetkin, 2009: Buoyancy Effects in a Strat-
782 ified Ekman Layer. *Journal of Physical Oceanography*, **39** (10), 2581–2599, doi:10.1175/
783 2009JPO4130.1, URL <http://journals.ametsoc.org/doi/abs/10.1175/2009JPO4130.1>.

- 784 McWilliams, J. C., and J. M. Restrepo, 1999: The wave-driven ocean circulation. *Journal of Phys-*
785 *ical Oceanography*, **29** (10), 2523–2540, URL [http://journals.ametsoc.org/doi/abs/10.1175/](http://journals.ametsoc.org/doi/abs/10.1175/1520-0485(1999)029%3C2523%3ATWDOC%3E2.0.CO%3B2)
786 [1520-0485\(1999\)029%3C2523%3ATWDOC%3E2.0.CO%3B2](http://journals.ametsoc.org/doi/abs/10.1175/1520-0485(1999)029%3C2523%3ATWDOC%3E2.0.CO%3B2).
- 787 McWilliams, J. C., P. P. Sullivan, and C.-H. Moeng, 1997: Langmuir turbulence in the ocean.
788 *Journal of Fluid Mechanics*, **334**, 1–30.
- 789 Miles, J., 1994: Analytical solutions for the Ekman layer. *Boundary-Layer Meteorology*, **67** (1-2),
790 1–10, doi:10.1007/BF00705505, URL <http://link.springer.com/10.1007/BF00705505>.
- 791 Nagai, T., A. Tandon, and D. L. Rudnick, 2006: Two-dimensional ageostrophic secondary cir-
792 culation at ocean fronts due to vertical mixing and large-scale deformation. *Journal of Geo-*
793 *physical Research*, **111** (C9), doi:10.1029/2005JC002964, URL [http://doi.wiley.com/10.1029/](http://doi.wiley.com/10.1029/2005JC002964)
794 [2005JC002964](http://doi.wiley.com/10.1029/2005JC002964).
- 795 Niiler, P. P., 1969: On the Ekman divergence in an oceanic jet. *Journal of Geophysical Re-*
796 *search*, **74** (28), 7048–7052, doi:10.1029/JC074i028p07048, URL [http://doi.wiley.com/10.](http://doi.wiley.com/10.1029/JC074i028p07048)
797 [1029/JC074i028p07048](http://doi.wiley.com/10.1029/JC074i028p07048).
- 798 O'Brien, J. J., 1970: A Note on the Vertical Structure of the Eddy Exchange Coefficient in
799 the Planetary Boundary Layer. *Journal of the Atmospheric Sciences*, **27** (8), 1213–1215, doi:
800 [10.1175/1520-0469\(1970\)027\(1213:ANOTVS\)2.0.CO;2](http://journals.ametsoc.org/doi/abs/10.1175/1520-0469(1970)027(1213:ANOTVS)2.0.CO;2), URL [http://journals.ametsoc.org/doi/](http://journals.ametsoc.org/doi/abs/10.1175/1520-0469(1970)027(1213:ANOTVS)2.0.CO;2)
801 [abs/10.1175/1520-0469\(1970\)027\(1213:ANOTVS\)2.0.CO;2](http://journals.ametsoc.org/doi/abs/10.1175/1520-0469(1970)027(1213:ANOTVS)2.0.CO;2), URL [http://journals.ametsoc.org/doi/](http://journals.ametsoc.org/doi/abs/10.1175/1520-0469(1970)027(1213:ANOTVS)2.0.CO;2)
[abs/10.1175/1520-0469\(1970\)027\(1213:ANOTVS\)2.0.CO;2](http://journals.ametsoc.org/doi/abs/10.1175/1520-0469(1970)027(1213:ANOTVS)2.0.CO;2).
- 802 Parmhed, O., I. Kos, and B. Grisogono, 2005: An improved Ekman layer approximation for
803 smooth eddy diffusivity profiles. *Boundary-layer meteorology*, **115** (3), 399–407, URL [http://](http://link.springer.com/article/10.1007/s10546-004-5940-0)
804 link.springer.com/article/10.1007/s10546-004-5940-0.

- 805 Peters, H., M. C. Gregg, and J. M. Toole, 1988: On the parameterization of equatorial turbulence.
806 *Journal of Geophysical Research*, **93 (C2)**, 1199, doi:10.1029/JC093iC02p01199, URL <http://doi.wiley.com/10.1029/JC093iC02p01199>.
807
- 808 Pollard, R. T., and L. A. Regier, 1992: Vorticity and Vertical Circulation at an Ocean Front.
809 *Journal of Physical Oceanography*, **22 (6)**, 609–625, doi:10.1175/1520-0485(1992)022<0609:
810 VAVCAA>2.0.CO;2, URL <http://journals.ametsoc.org/doi/abs/10.1175/1520-0485%281992%29022%3C0609%3AVAVCAA%3E2.0.CO%3B2>.
811
- 812 Pollard, R. T., P. B. Rhines, and R. O. R. Y. Thompson, 1973: The deepening of the wind-Mixed
813 layer. *Geophysical Fluid Dynamics*, **4 (1)**, 381–404, doi:10.1080/03091927208236105, URL
814 <http://www.tandfonline.com/doi/abs/10.1080/03091927208236105>.
- 815 Polton, J. A., Y.-D. Lenn, S. Elipot, T. K. Chereskin, and J. Sprintall, 2013: Can Drake Pas-
816 sage Observations Match Ekman’s Classic Theory? *Journal of Physical Oceanography*, **43 (8)**,
817 1733–1740, URL <http://journals.ametsoc.org/doi/abs/10.1175/JPO-D-13-034.1>.
- 818 Polton, J. A., D. M. Lewis, and S. E. Belcher, 2005: The role of wave-induced Coriolis-Stokes
819 forcing on the wind-driven mixed layer. *Journal of Physical Oceanography*, **35 (4)**, 444–457,
820 URL <http://journals.ametsoc.org/doi/abs/10.1175/JPO2701.1>.
- 821 Ponte, A. L., P. Klein, X. Capet, P.-Y. Le Traon, B. Chapron, and P. Lherminier, 2013: Diagnosing
822 Surface Mixed Layer Dynamics from High-Resolution Satellite Observations: Numerical In-
823 sights. *Journal of Physical Oceanography*, **43 (7)**, 1345–1355, doi:10.1175/JPO-D-12-0136.1,
824 URL <http://journals.ametsoc.org/doi/abs/10.1175/JPO-D-12-0136.1>.
- 825 Price, J. F., and M. A. Sundermeyer, 1999: Stratified Ekman layers. *Journal of Geophysical*
826 *Research*, **104 (C9)**, 20 467, doi:10.1029/1999JC900164, URL <http://doi.wiley.com/10.1029/>

827 1999JC900164.

828 Price, J. F., R. A. Weller, and R. Pinkel, 1986: Diurnal cycling: Observations and models of the
829 upper ocean response to diurnal heating, cooling, and wind mixing. *Journal of Geophysical*
830 *Research*, **91 (C7)**, 8411, doi:10.1029/JC091iC07p08411, URL [http://doi.wiley.com/10.1029/
831 JC091iC07p08411](http://doi.wiley.com/10.1029/JC091iC07p08411).

832 Price, J. F., R. A. Weller, and R. R. Schudlich, 1987: Wind-driven ocean currents and Ekman trans-
833 port. *Science*, **238 (4833)**, 1534–1538, URL [http://www.icess.ucsb.edu/~davey/TRANSFER/
834 Price_etal_Ekman.pdf](http://www.icess.ucsb.edu/~davey/TRANSFER/Price_etal_Ekman.pdf).

835 Raschle, N., and F. Ardhuin, 2009: Drift and mixing under the ocean surface revisited: Stratified
836 conditions and model-data comparisons. *Journal of Geophysical Research*, **114 (C2)**, doi:10.
837 1029/2007JC004466, URL <http://doi.wiley.com/10.1029/2007JC004466>.

838 Raschle, N., and F. Ardhuin, 2013: A global wave parameter database for geophysical applications.
839 Part 2: Model validation with improved source term parameterization. *Ocean Modelling*, **70**,
840 174–188, doi:10.1016/j.ocemod.2012.12.001, URL [http://linkinghub.elsevier.com/retrieve/pii/
841 S1463500312001709](http://linkinghub.elsevier.com/retrieve/pii/S1463500312001709).

842 Raschle, N., F. Ardhuin, P. Queffelec, and D. Croiz-Fillon, 2008: A global wave parame-
843 ter database for geophysical applications. Part 1: Wave-current-turbulence interaction param-
844 eters for the open ocean based on traditional parameterizations. *Ocean Modelling*, **25 (3-4)**,
845 154–171, doi:10.1016/j.ocemod.2008.07.006, URL [http://linkinghub.elsevier.com/retrieve/pii/
846 S1463500308001017](http://linkinghub.elsevier.com/retrieve/pii/S1463500308001017).

847 Roach, C. J., H. E. Phillips, N. L. Bindoff, and S. R. Rintoul, 2015: Detecting and Characterizing
848 Ekman Currents in the Southern Ocean. *Journal of Physical Oceanography*, **45 (5)**, 1205–1223,

849 URL <http://journals.ametsoc.org/doi/abs/10.1175/JPO-D-14-0115.1>.

850 Rudnick, D. L., 1996: Intensive surveys of the Azores Front: 2. Inferring the geostrophic and verti-
851 cal velocity fields. *Journal of Geophysical Research*, **101** (C7), 16 291, doi:10.1029/96JC01144,
852 URL <http://doi.wiley.com/10.1029/96JC01144>.

853 Saha, S., and Coauthors, 2006: The NCEP Climate Forecast System. *Journal of Climate*,
854 **19** (15), 3483–3517, doi:10.1175/JCLI3812.1, URL <http://journals.ametsoc.org/doi/abs/10.1175/JCLI3812.1>.

856 Samelson, R. M., 1993: Linear instability of a mixed-layer front. *Journal of Geophysical Research*,
857 **98** (C6), 10 195, doi:10.1029/93JC00457, URL <http://doi.wiley.com/10.1029/93JC00457>.

858 Schudlich, R. R., and J. F. Price, 1998: Observations of Seasonal Variation in the Ekman
859 Layer. *Journal of Physical Oceanography*, **28** (6), 1187–1204, doi:10.1175/1520-0485(1998)
860 028<1187:OOSVIT>2.0.CO;2, URL [http://journals.ametsoc.org/doi/abs/10.1175/1520-0485%
861 281998%29028%3C1187%3AOOSVIT%3E2.0.CO%3B2](http://journals.ametsoc.org/doi/abs/10.1175/1520-0485%281998%29028%3C1187%3AOOSVIT%3E2.0.CO%3B2).

862 Smith, J. A., 1992: Observed growth of Langmuir circulation. *Journal of Geophysical Research*,
863 **97** (C4), 5651, doi:10.1029/91JC03118, URL <http://doi.wiley.com/10.1029/91JC03118>.

864 Smyth, W. D., J. N. Moum, L. Li, and S. A. Thorpe, 2013: Diurnal Shear Instability, the
865 Descent of the Surface Shear Layer, and the Deep Cycle of Equatorial Turbulence. *Jour-
866 nal of Physical Oceanography*, **43** (11), 2432–2455, doi:10.1175/JPO-D-13-089.1, URL [http:
867 //journals.ametsoc.org/doi/abs/10.1175/JPO-D-13-089.1](http://journals.ametsoc.org/doi/abs/10.1175/JPO-D-13-089.1).

868 Soloviev, A., and R. Lukas, 2014: *The near-surface layer of the ocean: structure, dynamics and
869 applications*. Second edition ed., No. volume 48, Atmospheric and oceanographic sciences li-
870 brary, Springer, Dordrecht.

- 871 Stern, M. E., 1965: Interaction of a uniform wind stress with a geostrophic vortex. *Deep Sea*
872 *Research and Oceanographic Abstracts*, **12 (3)**, 355–367, doi:10.1016/0011-7471(65)90007-0,
873 URL <http://linkinghub.elsevier.com/retrieve/pii/0011747165900070>.
- 874 Stommel, H., 1960: Wind-drift near the equator. *Deep Sea Research (1953)*, **6**, 298–
875 302, doi:10.1016/0146-6313(59)90088-7, URL [http://linkinghub.elsevier.com/retrieve/pii/](http://linkinghub.elsevier.com/retrieve/pii/0146631359900887)
876 [0146631359900887](http://linkinghub.elsevier.com/retrieve/pii/0146631359900887).
- 877 Sullivan, P. P., and J. C. McWilliams, 2010: Dynamics of Winds and Currents Cou-
878 pled to Surface Waves. *Annual Review of Fluid Mechanics*, **42 (1)**, 19–42, doi:10.1146/
879 [annurev-fluid-121108-145541](https://doi.org/10.1146/annurev-fluid-121108-145541).
- 880 Tan, Z.-M., 2001: An Approximate Analytical Solution For The Baroclinic And Variable
881 Eddy Diffusivity Semi-Geostrophic Ekman Boundary Layer. *Boundary-Layer Meteorology*,
882 **98 (3)**, 361–385, doi:10.1023/A:1018708726112, URL [http://link.springer.com/article/10.1023/](http://link.springer.com/article/10.1023/A%3A1018708726112)
883 [A%3A1018708726112](http://link.springer.com/article/10.1023/A%3A1018708726112).
- 884 Thomas, L., and R. Ferrari, 2008: Friction, Frontogenesis, and the Stratification of the Sur-
885 face Mixed Layer. *Journal of Physical Oceanography*, **38 (11)**, 2501–2518, doi:10.1175/
886 [2008JPO3797.1](https://doi.org/10.1175/2008JPO3797.1), URL <http://journals.ametsoc.org/doi/abs/10.1175/2008JPO3797.1>.
- 887 Thomas, L. N., 2005: Destruction of Potential Vorticity by Winds. *Journal of Physical Oceanog-*
888 *raphy*, **35 (12)**, 2457–2466, doi:10.1175/JPO2830.1, URL [http://journals.ametsoc.org/doi/abs/](http://journals.ametsoc.org/doi/abs/10.1175/JPO2830.1)
889 [10.1175/JPO2830.1](http://journals.ametsoc.org/doi/abs/10.1175/JPO2830.1).
- 890 Thomas, L. N., 2007: Dynamical constraints on the extreme low values of the potential vorticity in
891 the ocean. *Proc. 15th Aha Huliko a Hawaiian Winter Workshop*, 117–124, URL [https://pangea.](https://pangea.stanford.edu/~leift/Thomas_Aha_2007.pdf)
892 [stanford.edu/~leift/Thomas_Aha_2007.pdf](https://pangea.stanford.edu/~leift/Thomas_Aha_2007.pdf).

- 893 Thomas, L. N., and C. M. Lee, 2005: Intensification of Ocean Fronts by Down-Front Winds.
894 *Journal of Physical Oceanography*, **35** (6), 1086–1102, doi:10.1175/JPO2737.1, URL [http://](http://journals.ametsoc.org/doi/abs/10.1175/JPO2737.1)
895 journals.ametsoc.org/doi/abs/10.1175/JPO2737.1.
- 896 Thomas, L. N., and P. B. Rhines, 2002: Nonlinear stratified spin-up. *Journal of Fluid Mechanics*,
897 **473**, 211–244.
- 898 Thompson, L., 2000: Ekman layers and two-dimensional frontogenesis in the upper ocean.
899 *Journal of Geophysical Research*, **105** (C3), 6437, doi:10.1029/1999JC900336, URL [http://](http://doi.wiley.com/10.1029/1999JC900336)
900 doi.wiley.com/10.1029/1999JC900336.
- 901 Welander, P., 1957: Wind Action on a Shallow Sea: Some Generalizations of Ekman's Theory. *Tel-*
902 *lus*, **9** (1), 45–52, doi:10.1111/j.2153-3490.1957.tb01852.x, URL [http://tellusa.net/index.php/](http://tellusa.net/index.php/tellusa/article/view/9070)
903 [tellusa/article/view/9070](http://tellusa.net/index.php/tellusa/article/view/9070).
- 904 Wenegrat, J. O., and M. J. McPhaden, 2015: Dynamics of the surface layer diurnal cycle in the
905 equatorial Atlantic Ocean (0, 23W). *Journal of Geophysical Research: Oceans*, **120** (1), 563–
906 581, doi:10.1002/2014JC010504, URL <http://doi.wiley.com/10.1002/2014JC010504>.
- 907 Wenegrat, J. O., M. J. McPhaden, and R.-C. Lien, 2014: Wind stress and near-surface shear in the
908 equatorial Atlantic Ocean: Wenegrat et al.: Wind Stress and Near-Surface Shear. *Geophysical*
909 *Research Letters*, **41** (4), 1226–1231, doi:10.1002/2013GL059149, URL [http://doi.wiley.com/](http://doi.wiley.com/10.1002/2013GL059149)
910 [10.1002/2013GL059149](http://doi.wiley.com/10.1002/2013GL059149).
- 911 Wijffels, S., E. Firing, and H. Bryden, 1994: Direct Observations of the Ekman Balance at
912 10N in the Pacific. *Journal of Physical Oceanography*, **24** (7), 1666–1679, doi:10.1175/
913 1520-0485(1994)024<1666:DOOTEB>2.0.CO;2, URL [http://journals.ametsoc.org/doi/abs/10.](http://journals.ametsoc.org/doi/abs/10.1175/1520-0485%281994%29024%3C1666%3ADOOTEB%3E2.0.CO%3B2)
914 [1175/1520-0485%281994%29024%3C1666%3ADOOTEB%3E2.0.CO%3B2](http://journals.ametsoc.org/doi/abs/10.1175/1520-0485%281994%29024%3C1666%3ADOOTEB%3E2.0.CO%3B2).

- 915 Wu, R., and W. Blumen, 1982: An Analysis of Ekman Boundary Layer Dynamics
916 Incorporating the Geostrophic Momentum Approximation. *Journal of the Atmospheric*
917 *Sciences*, **39** (8), 1774–1782, doi:10.1175/1520-0469(1982)039<1774:AAOEBL>2.0.CO;
918 2, URL [http://journals.ametsoc.org/doi/abs/10.1175/1520-0469%281982%29039%3C1774%
919 3AAAOEBL%3E2.0.CO%3B2](http://journals.ametsoc.org/doi/abs/10.1175/1520-0469%281982%29039%3C1774%3AAAOEBL%3E2.0.CO%3B2).
- 920 Xu, Z., and A. J. Bowen, 1994: Wave-and wind-driven flow in water of finite depth. *Journal of*
921 *physical oceanography*, **24** (9), 1850–1866, URL [http://journals.ametsoc.org/doi/abs/10.1175/
922 1520-0485\(1994\)024%3C1850:WAWDFI%3E2.0.CO%3B2](http://journals.ametsoc.org/doi/abs/10.1175/1520-0485(1994)024%3C1850:WAWDFI%3E2.0.CO%3B2).
- 923 Zikanov, O., D. N. Slinn, and M. R. Dhanak, 2003: Large-eddy simulations of the wind-
924 induced turbulent Ekman layer. *Journal of Fluid Mechanics*, **495**, 343–368, doi:10.1017/
925 S0022112003006244, URL http://www.journals.cambridge.org/abstract_S0022112003006244.

926 **LIST OF TABLES**

927 **Table 1.** Parameters for equations (19-23). 46

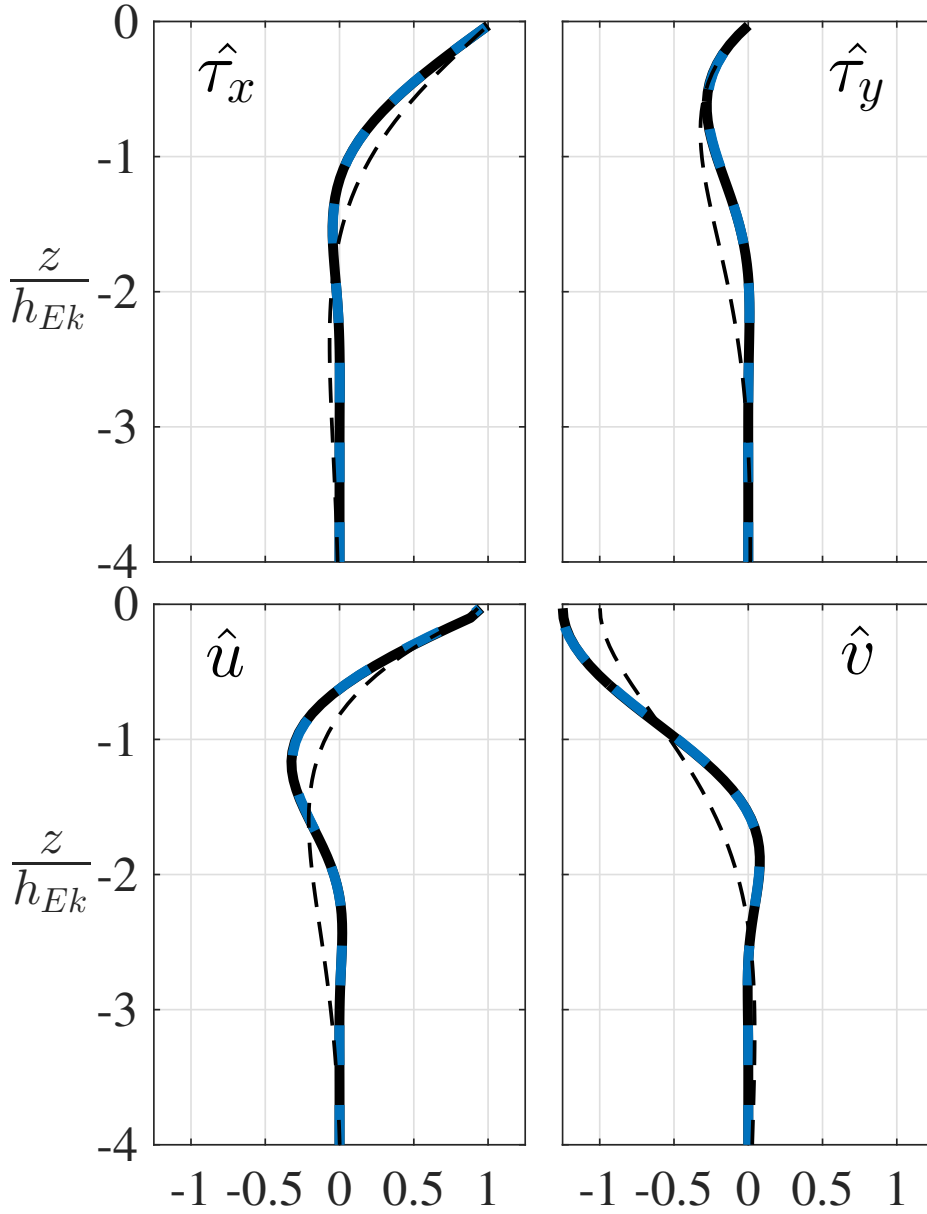
TABLE 1. Parameters for equations (19-23).

<i>Parameter</i>	<i>Value</i>	Physical Interpretation
b_f	$-0.6g/\rho_0$	Buoyancy change across front
b_b	$bf/2$	Buoyancy change across thermocline
α	-1.185	Horizontal scaling factor
z_0	0.75	Vertical position
x_0	1	Horizontal position
d_0	0.125	Horizontal scale
d_1	0.125	Vertical scale
f	$6.88 \times 10^{-5} s^{-1}$	Coriolis frequency
A_{v0}	$3 \times 10^{-2} m^2 s^{-1}$	Eddy viscosity magnitude
A_{vb}	$1 \times 10^{-4} m^2 s^{-1}$	Background viscosity
h_0	0.84	Turbulent boundary layer depth
δ_h	0.05	Across front change in boundary layer depth
ζ_0	5×10^{-3}	Regularization constant

928 **LIST OF FIGURES**

- 929 **Fig. 1.** Example profiles of stress and velocity for an exponentially decaying eddy viscosity, $A_v = A_{v0}e^{z/h_{Ek}}$ for numeric (solid black) and WKB solution given by equation (7) (dashed blue), and for constant eddy viscosity $A_v = A_{v0}$ (thin dashed black). Top row, stress profiles, normalized by the surface wind stress value, $\hat{\tau} = \tau(z)/|\tau_w|$. Bottom row, velocity profiles, normalized by, $\hat{u} = u(z)|\tau_w/(\rho f h_{Ek}(0))|^{-1}$. The WKB solution overlaps the numerical solution to within the thickness of the plotted line. 49
- 935 **Fig. 2.** Green’s function, (9), for a point source located at z_0 in a boundary layer of depth $h = 6h_{Ek}$ 50
- 936 **Fig. 3.** Schematics of the ageostrophic flow induced by a horizontal buoyancy gradient, with thin lines indicating density contours. a) Uniform viscosity and buoyancy gradient leads to a downgradient ageostrophic flow in the near-surface Ekman layer, and upgradient flow in a bottom Ekman layer. b) Uniform viscosity and linearly decaying buoyancy gradient leads to a downgradient ageostrophic flow in the Ekman layer, and a uniform weak up-gradient flow throughout the remainder of the layer. c) linearly decaying viscosity and uniform buoyancy gradient leads to a similar pattern of flow as in the middle panel. Figure is based on Thomas and Ferrari (2008), their Figure 1. 51
- 944 **Fig. 4.** Stress and ageostrophic velocity for a zonal surface wind stress, $\tau_w = 0.1 \text{ Nm}^{-2}$, in the presence of a downwind wave field with Stokes velocity amplitude $U_0 = 0.22 \text{ ms}^{-1}$ and depth scale, $h_s = 3.4 \text{ m}$ (Komen 1996). a) Hodograph of total stress (black), wind-forced component (blue), component forced by the effective surface stress arising from the Coriolis-Stokes stress (solid red), and the Coriolis-Stokes stress (dashed red). b) Zonal ageostrophic velocity profile with components as in (a), c) as in (b) but for meridional velocity. In b and c the Ekman depth (solid black) and h_s (dashed black) are indicated. 52
- 951 **Fig. 5.** Schematic of the components of the frictional ageostrophic response to a horizontal buoyancy gradient, with contours of constant ρ shown in gray. The geostrophic stress is rotated by an angle λ from the geostrophic shear, which points along lines of constant ρ . The divergence of this geostrophic stress drives an ageostrophic velocity, u_{BL} , and transport U_{BL}^T , rotated 90° to the right (N. Hemisphere). Geostrophic stress at the surface drives an Ekman response, through an effective surface stress $-\tau_{geo}$, with associated velocities u_{Ek} , and transport U_{Ek}^T . The surface velocity is given by $u_{surf} = u_{BL}(0) + u_{Ek}(0)$. Vectors are not to scale. 53
- 959 **Fig. 6.** Contour plots of λ ($^\circ$, positive solid, negative dashed), the angle of the geostrophic stress relative to the direction of the geostrophic shear, as defined in the text by (16), evaluated at $z = 0$. Left panel: Linear A_v ($A_v(z) = A_{v0}(1 + \frac{z}{h_{Av}})$) and linear ∇b ($\nabla b(z) = B_0(1 + \frac{z}{h_\rho})$), right panel: modified Gaussian A_v ($A_v(z) = A_{v0}(\frac{z}{h_{Av}} + 0.25)\exp[-\frac{1}{2}(\frac{z}{h_{Av}})^2 + \frac{1}{2}]$), as discussed in Appendix B, and exponential $\nabla b(z)$ ($\nabla b(z) = B_0 e^{\frac{z}{h_\rho}}$). In both plots $h_{Ek} = \sqrt{2A_{v0}/f}$, and positive parameter values indicate fields which decay downwards. 54
- 965 **Fig. 7.** Across-front sections of the idealized two-dimensional front discussed in section 4, with contours of constant ρ indicated in solid black. Upper left: along-front geostrophic velocity, upper right: A_v , lower panel: frictional ageostrophic overturning streamfunction ($m^2 s^{-1}$, eq. 24), with contours of constant A_v in gray. 55
- 969 **Fig. 8.** Frictionally driven boundary layer vertical velocity. Top: Total vertical velocity, Middle: vertical velocity arising from the gradient in the horizontal buoyancy gradient, Bottom: ver-

971	tical velocity due to gradient in A_v . The dashed line indicates the turbulent surface boundary	
972	layer depth, defined by (23). Note reduced colorscale in bottom panel.	56
973	Fig. 9. Global climatology, 2001-2011, by seasons with months indicated in plot titles, for γ_{GEO} as	
974	defined in the text by equation (27).	57
975	Fig. 10. As in figure 9 but for γ_{CS} as defined in the text by equation (28).	58
976	Fig. 11. Zonal, and temporal, averages of γ_{GEO} and γ_{CS}	59
977	Fig. 12. Global area-weighted joint probability density function (PDF) of γ_{GEO} and γ_{CS} , center panel,	
978	estimated monthly from 2001-2011. Left panel shows the PDF of γ_{GEO} , lower panel the PDF	
979	of γ_{CS} . Climatological average values are indicated in the center panel for the locations of	
980	several previous Ekman layer studies, Long Term Upper Ocean Study ('x', Price et al.	
981	1987), Transpacific Hydrographic Survey (basin averaged, '◇', Wijffels et al. 1994), East-	
982	ern Boundary Current experiment ('+', Chereskin 1995), and 2°N, 140°W ('○', Cronin and	
983	Kessler 2009).	60
984	Fig. 13. Example single month estimate of γ_{GEO} and γ_{CS} , showing additional spatial detail not evi-	
985	dent in the climatological maps (figures 9, 10).	61
986	Fig. 14. Frictional flux of potential vorticity due to the wind-driven differential horizontal buoyancy	
987	advection across the Ekman layer. Numerical solutions of $f[u_{Ek} \cdot \nabla b]_{z=0}$ are plotted (solid)	
988	as a function of the eddy viscosity depth scale, where $A_v(z) = A_{v0}e^{z/h_{Av}}$. Values are nor-	
989	malized by (29). Also plotted is the scaling suggested by (30) (dashed), which overlaps the	
990	numerical solution for most of the parameter space.	62
991	Fig. B1. Vertical structure of A_v models considered in Appendix B. In each case the normalization is	
992	such that $h = 1$, $f = 1$, and $A_{v0} = Ek \times 1 \text{ m}^2 \text{ s}^{-1}$	63
993	Fig. B2. Accuracy of WKB approximation as a function of Ekman number for the A_v profiles shown	
994	in figure B1. Top panel is for wind-forcing, bottom panel for a vertically uniform horizontal	
995	buoyancy gradient. Errors are normalized according to (B5).	64



996 FIG. 1. Example profiles of stress and velocity for an exponentially decaying eddy viscosity, $A_v = A_{v0}e^{z/h_{Ek}}$
 997 for numeric (solid black) and WKB solution given by equation (7) (dashed blue), and for constant eddy vis-
 998 cosity $A_v = A_{v0}$ (thin dashed black). Top row, stress profiles, normalized by the surface wind stress value,
 999 $\hat{\tau} = \tau(z)/|\tau_w|$. Bottom row, velocity profiles, normalized by, $\hat{u} = u(z)/|\tau_w/(\rho f h_{Ek}(0))|^{-1}$. The WKB solution
 1000 overlaps the numerical solution to within the thickness of the plotted line.

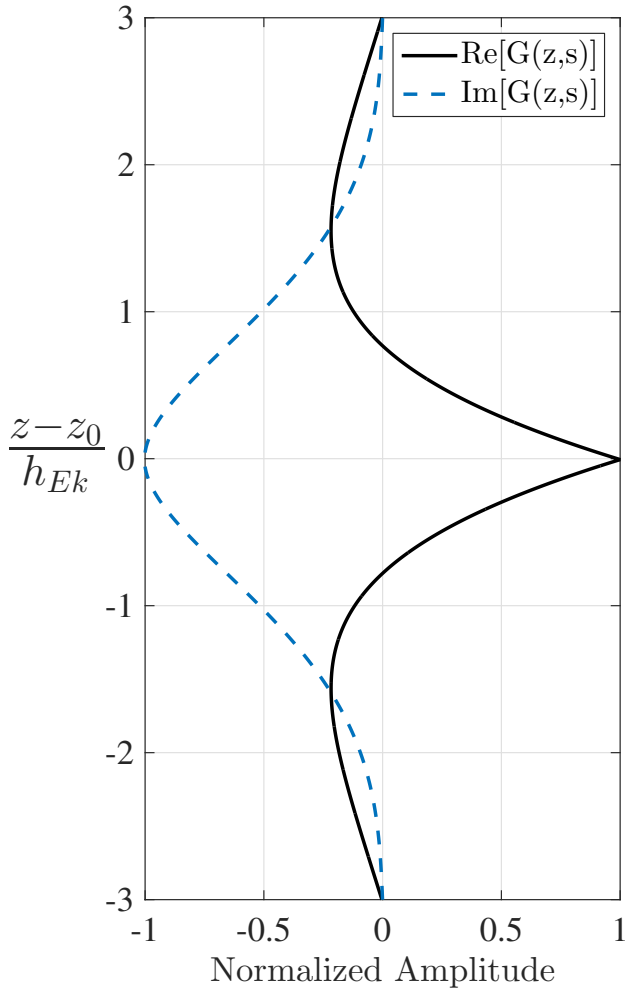
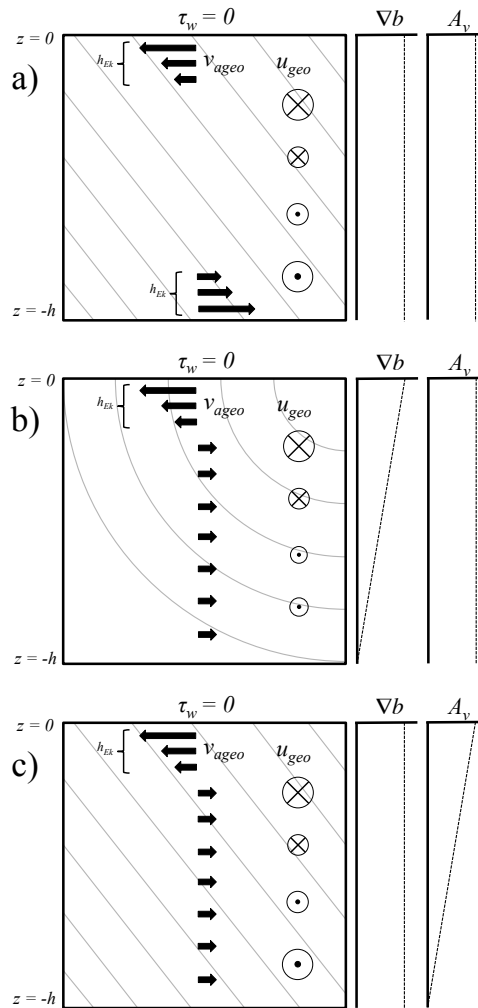
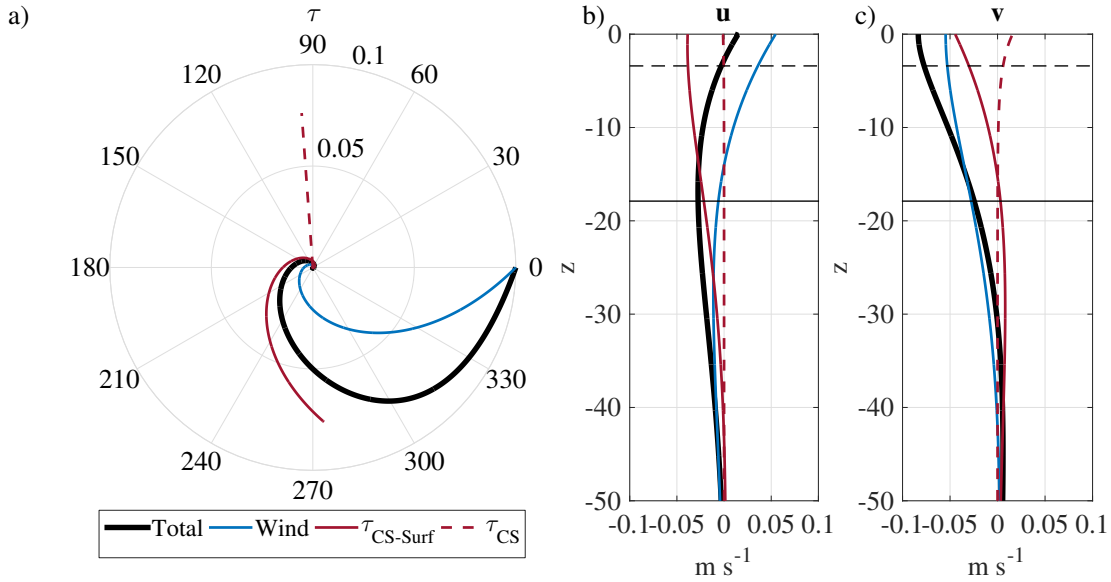


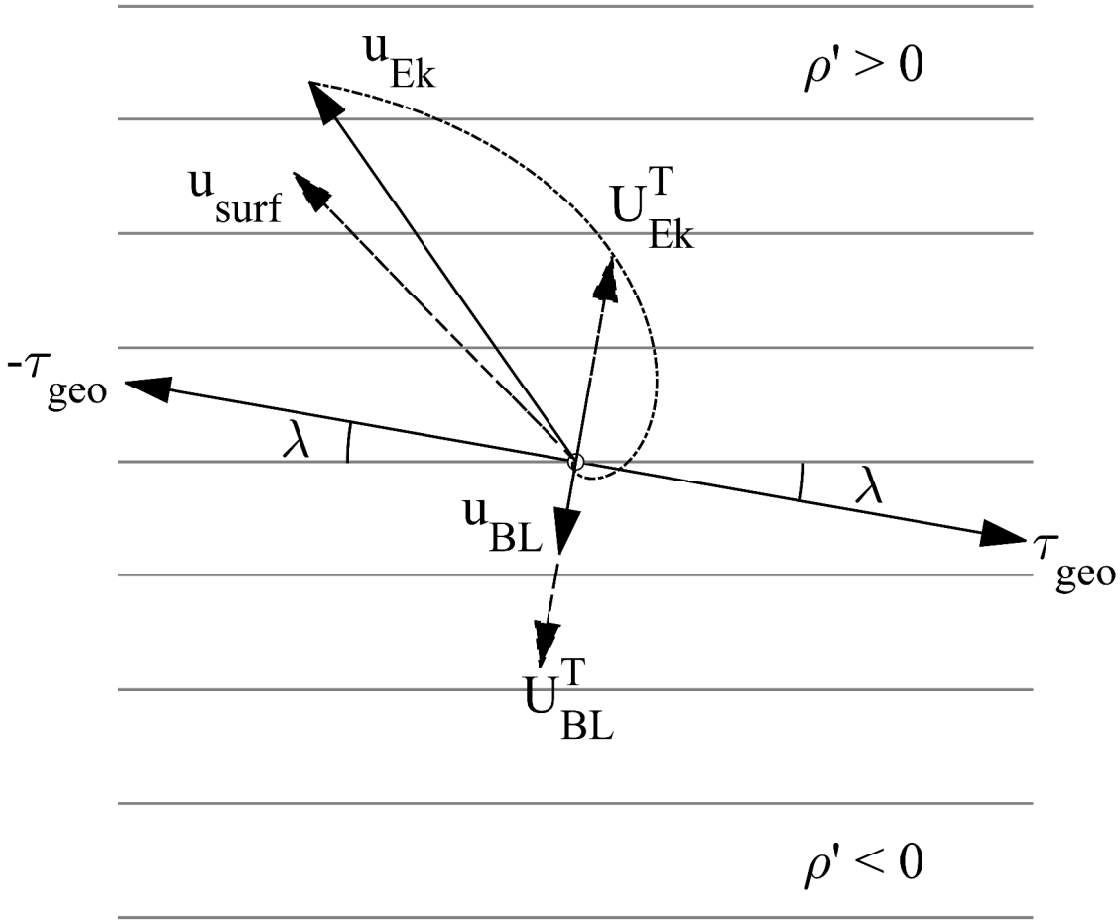
FIG. 2. Green's function, (9), for a point source located at z_0 in a boundary layer of depth $h = 6h_{Ek}$.



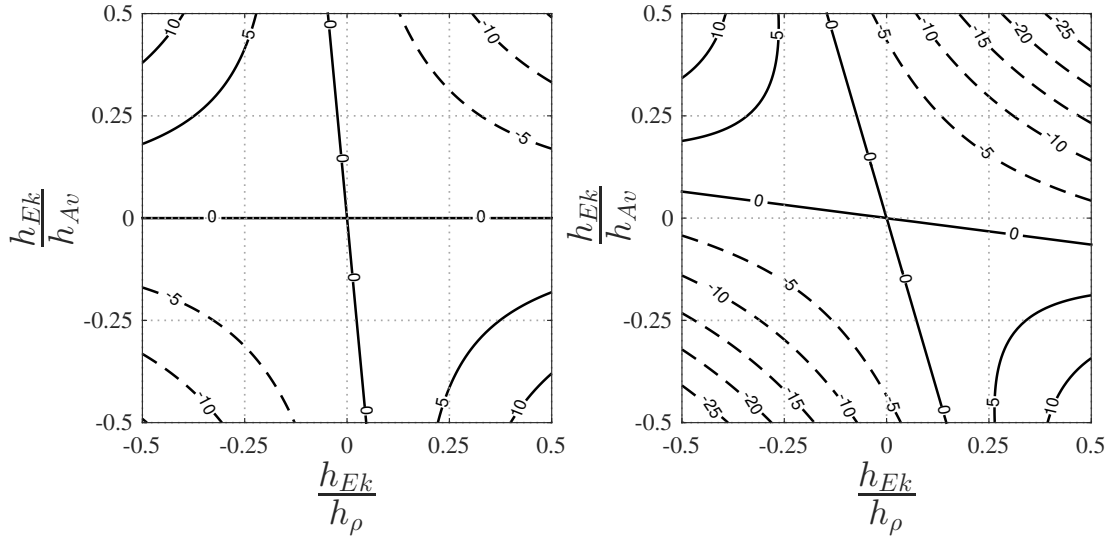
1001 FIG. 3. Schematics of the ageostrophic flow induced by a horizontal buoyancy gradient, with thin lines
 1002 indicating density contours. a) Uniform viscosity and buoyancy gradient leads to a downgradient ageostrophic
 1003 flow in the near-surface Ekman layer, and upgradient flow in a bottom Ekman layer. b) Uniform viscosity
 1004 and linearly decaying buoyancy gradient leads to a downgradient ageostrophic flow in the Ekman layer, and a
 1005 uniform weak up-gradient flow throughout the remainder of the layer. c) linearly decaying viscosity and uniform
 1006 buoyancy gradient leads to a similar pattern of flow as in the middle panel. Figure is based on Thomas and Ferrari
 1007 (2008), their Figure 1.



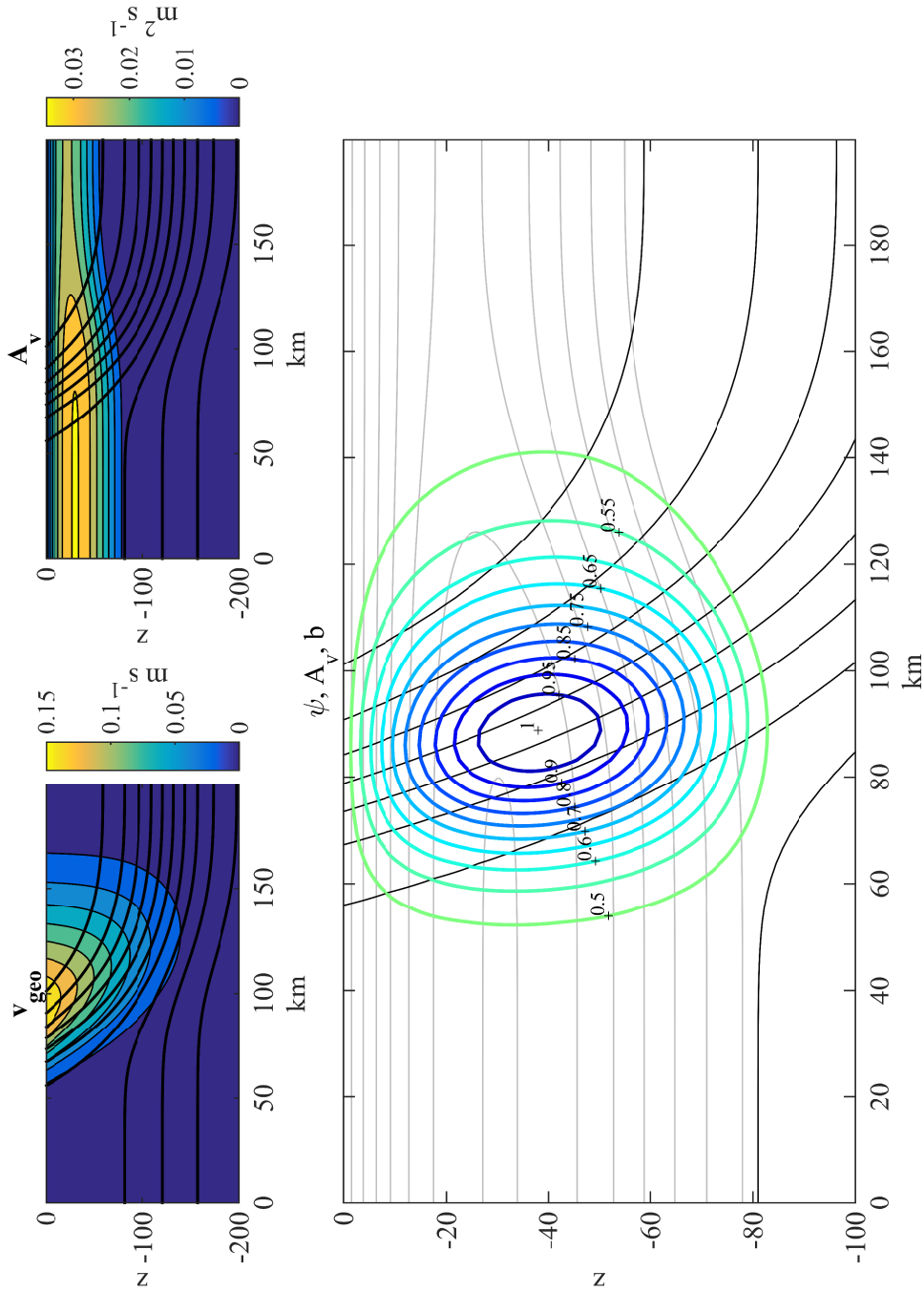
1008 FIG. 4. Stress and ageostrophic velocity for a zonal surface wind stress, $\tau_w = 0.1 \text{ Nm}^{-2}$, in the presence of
 1009 a downwind wave field with Stokes velocity amplitude $U_0 = 0.22 \text{ ms}^{-1}$ and depth scale, $h_s = 3.4 \text{ m}$ (Komen
 1010 1996). a) Hodograph of total stress (black), wind-forced component (blue), component forced by the effective
 1011 surface stress arising from the Coriolis-Stokes stress (solid red), and the Coriolis-Stokes stress (dashed red). b)
 1012 Zonal ageostrophic velocity profile with components as in (a), c) as in (b) but for meridional velocity. In b and
 1013 c the Ekman depth (solid black) and h_s (dashed black) are indicated.



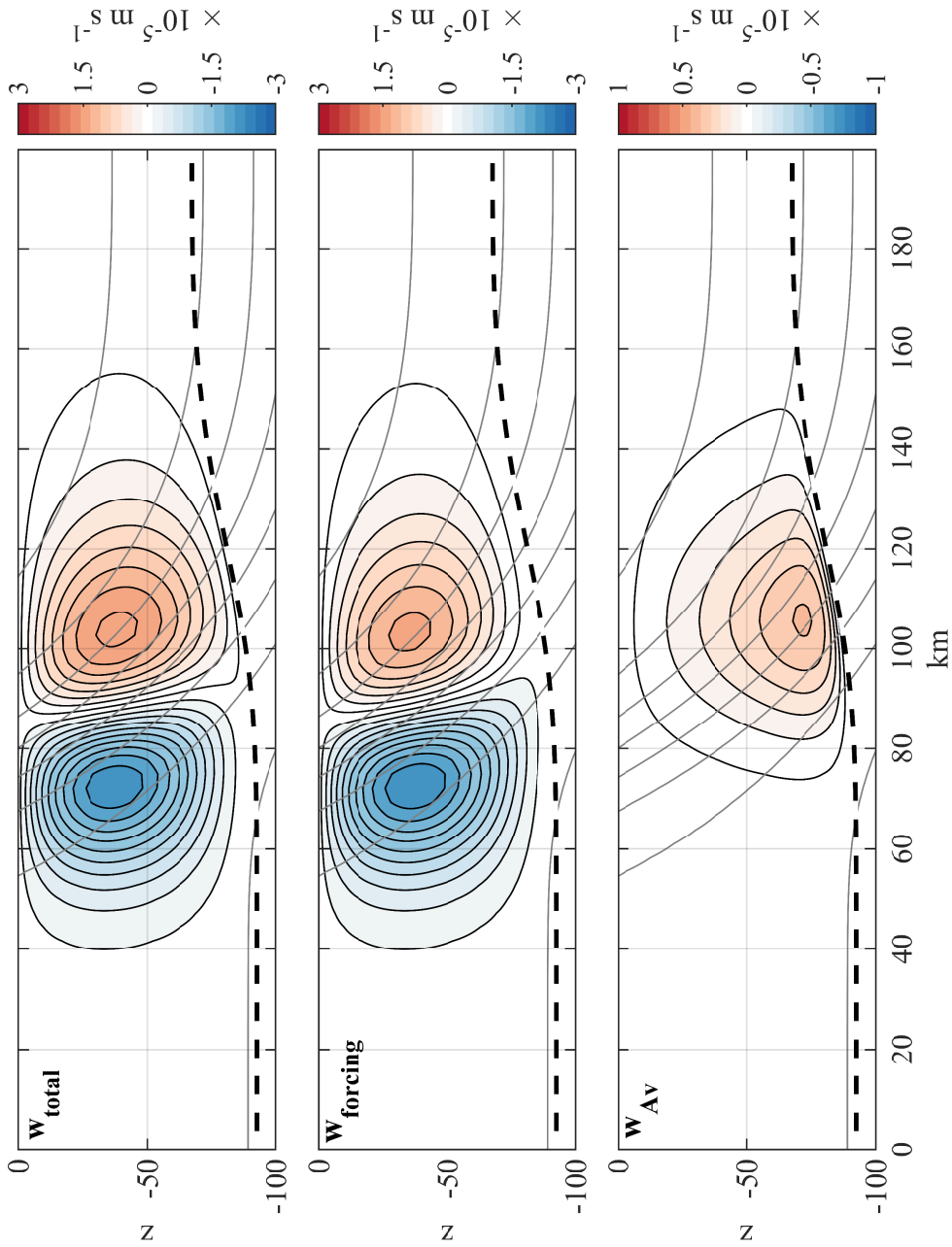
1014 FIG. 5. Schematic of the components of the frictional ageostrophic response to a horizontal buoyancy gradient,
 1015 with contours of constant ρ shown in gray. The geostrophic stress is rotated by an angle λ from the geostrophic
 1016 shear, which points along lines of constant ρ . The divergence of this geostrophic stress drives an ageostrophic
 1017 velocity, u_{BL} , and transport U_{BL}^T , rotated 90° to the right (N. Hemisphere). Geostrophic stress at the surface drives
 1018 an Ekman response, through an effective surface stress $-\tau_{geo}$, with associated velocities u_{Ek} , and transport U_{Ek}^T .
 1019 The surface velocity is given by $u_{surf} = u_{BL}(0) + u_{Ek}(0)$. Vectors are not to scale.



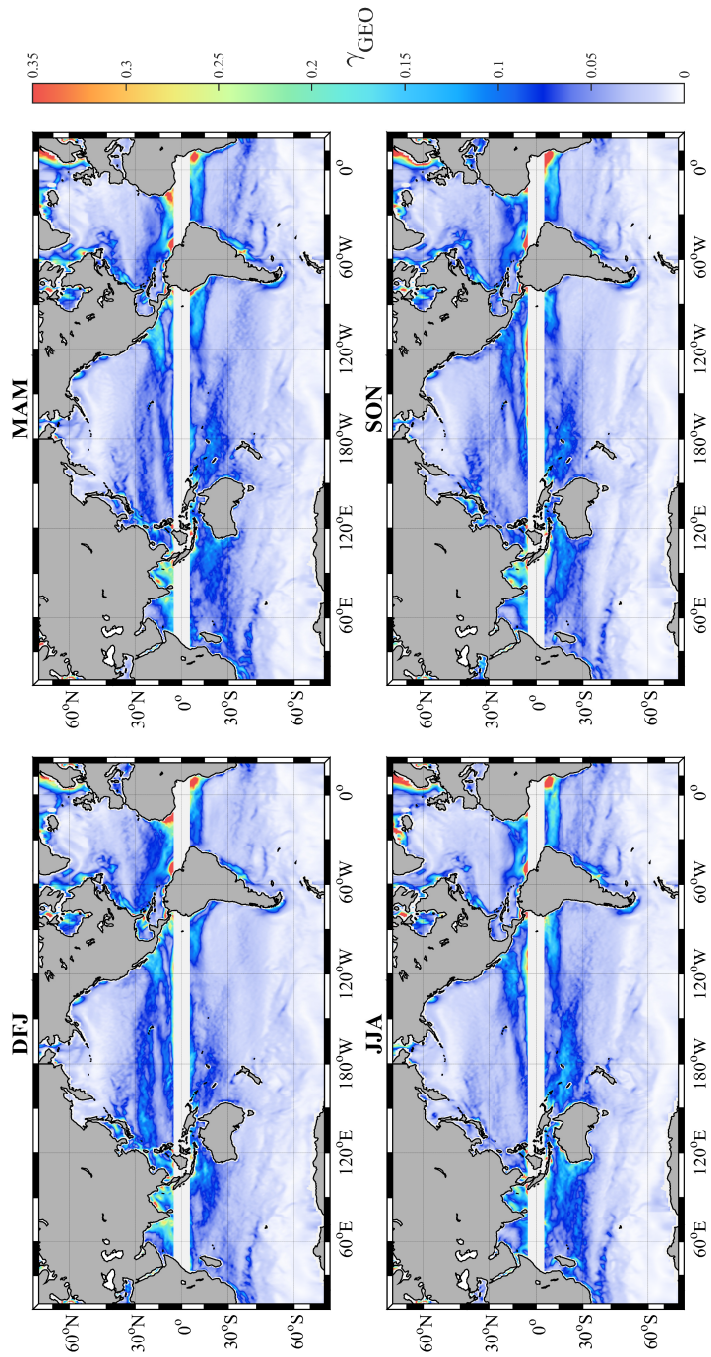
1020 FIG. 6. Contour plots of λ ($^\circ$, positive solid, negative dashed), the angle of the geostrophic stress relative
 1021 to the direction of the geostrophic shear, as defined in the text by (16), evaluated at $z = 0$. Left panel: Linear
 1022 A_v ($A_v(z) = A_{v0}(1 + \frac{z}{h_{Av}})$) and linear ∇b ($\nabla b(z) = B_0(1 + \frac{z}{h_\rho})$), right panel: modified Gaussian A_v ($A_v(z) =$
 1023 $A_{v0}(\frac{z}{h_{Av}} + 0.25)\exp[-\frac{1}{2}(\frac{z}{h_{Av}})^2 + \frac{1}{2}]$), as discussed in Appendix B, and exponential $\nabla b(z)$ ($\nabla b(z) = B_0 e^{\frac{z}{h_\rho}}$). In
 1024 both plots $h_{Ek} = \sqrt{2A_{v0}/f}$, and positive parameter values indicate fields which decay downwards.



1025 FIG. 7. Across-front sections of the idealized two-dimensional front discussed in section 4, with contours of
 1026 constant ρ indicated in solid black. Upper left: along-front geostrophic velocity, upper right: A_v , lower panel:
 1027 frictional ageostrophic overturning streamfunction ($\text{m}^2 \text{s}^{-1}$, eq. 24), with contours of constant A_v in gray.



1028 FIG. 8. Frictionally driven boundary layer vertical velocity. Top: Total vertical velocity, Middle: vertical
 1029 velocity arising from the gradient in the horizontal buoyancy gradient, Bottom: vertical velocity due to gradient
 1030 in A_v . The dashed line indicates the turbulent surface boundary layer depth, defined by (23). Note reduced
 1031 colorscale in bottom panel.



1032 FIG. 9. Global climatology, 2001-2011, by seasons with months indicated in plot titles, for γ_{GEO} as defined
 1033 in the text by equation (27).

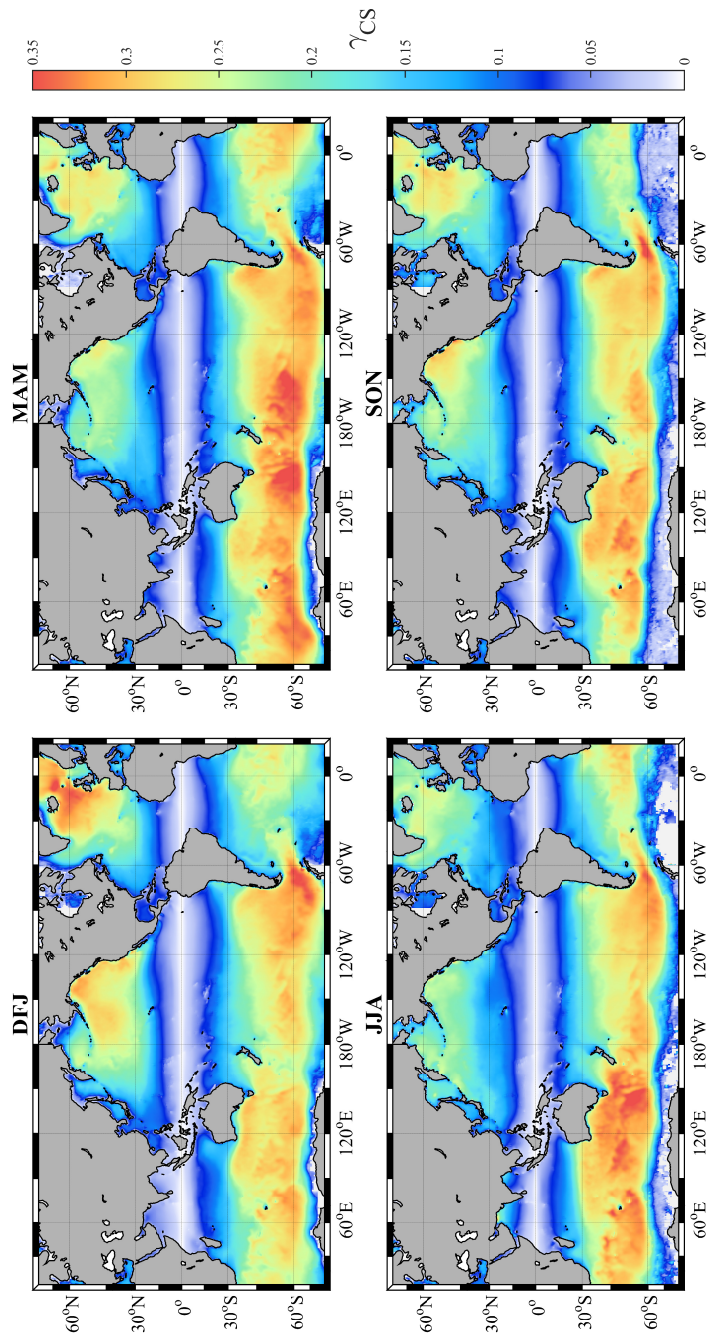


FIG. 10. As in figure 9 but for γ_{CS} as defined in the text by equation (28).

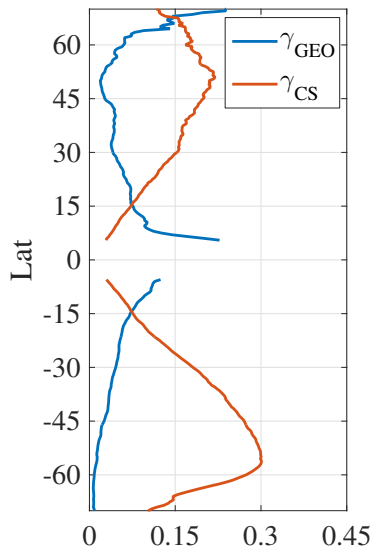
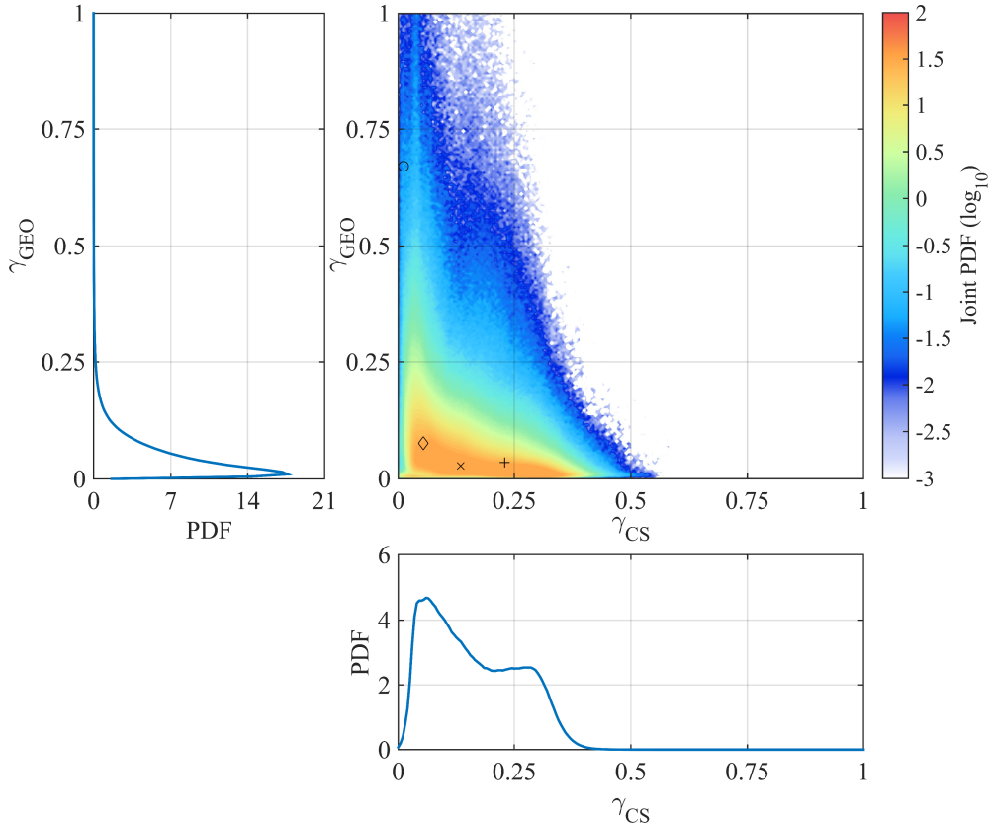
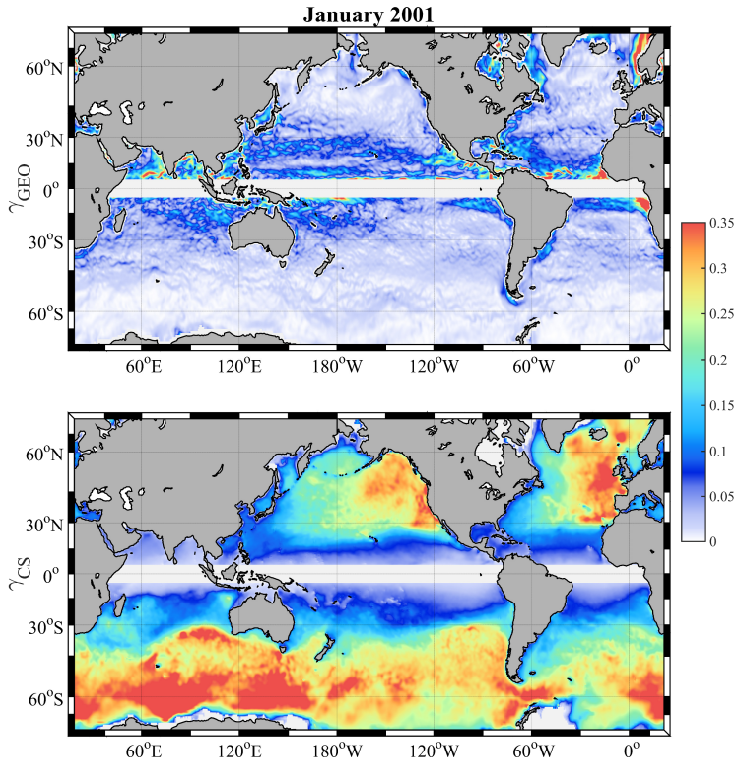


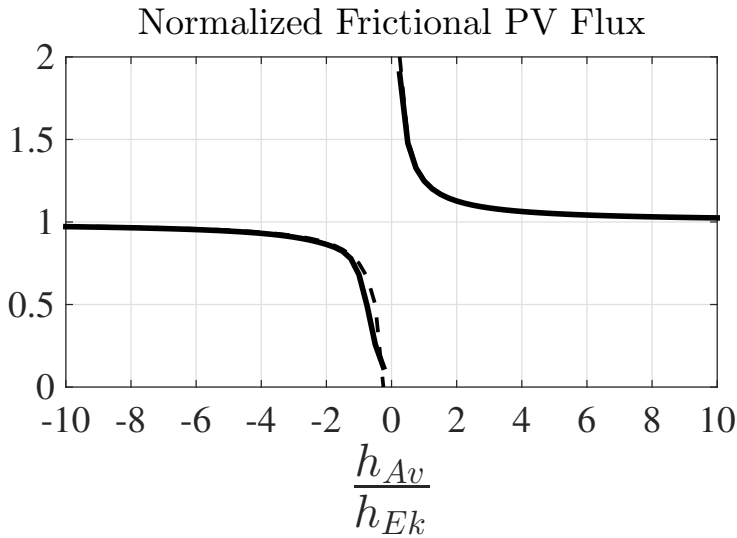
FIG. 11. Zonal, and temporal, averages of γ_{GEO} and γ_{CS} .



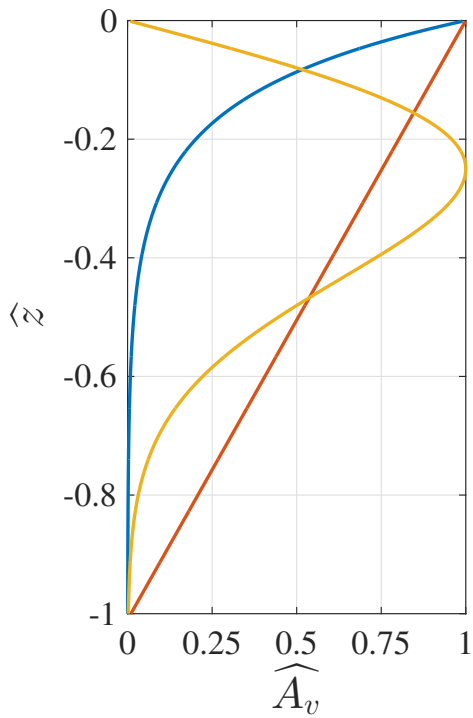
1034 FIG. 12. Global area-weighted joint probability density function (PDF) of γ_{GEO} and γ_{CS} , center panel, esti-
 1035 mated monthly from 2001-2011. Left panel shows the PDF of γ_{GEO} , lower panel the PDF of γ_{CS} . Climatological
 1036 average values are indicated in the center panel for the locations of several previous Ekman layer studies, Long
 1037 Term Upper Ocean Study ('x', Price et al. 1987), Transpacific Hydrographic Survey (basin averaged, ' \diamond ', Wijf-
 1038 fels et al. 1994), Eastern Boundary Current experiment ('+', Chereskin 1995), and 2°N , 140°W (' \circ ', Cronin and
 1039 Kessler 2009).



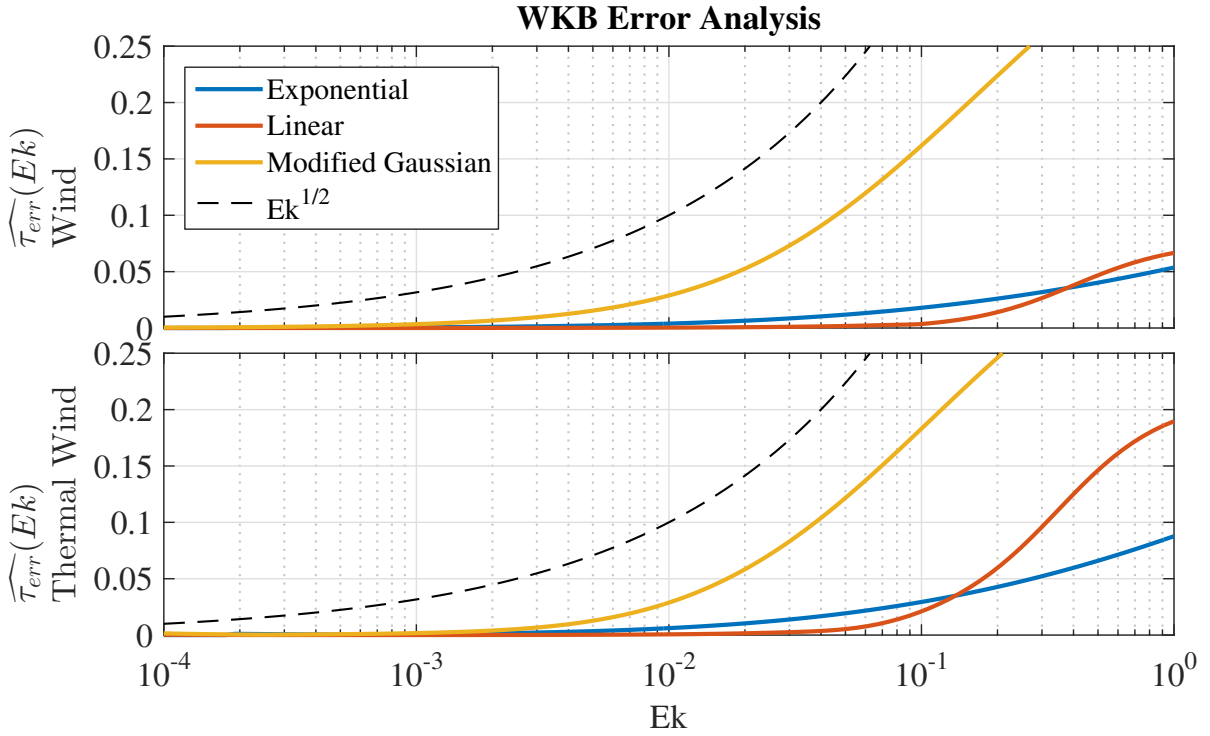
1040 FIG. 13. Example single month estimate of γ_{GEO} and γ_{CS} , showing additional spatial detail not evident in the
 1041 climatological maps (figures 9, 10).



1042 FIG. 14. Frictional flux of potential vorticity due to the wind-driven differential horizontal buoyancy advection
 1043 across the Ekman layer. Numerical solutions of $f[u_{Ek} \cdot \nabla b]_{z=0}$ are plotted (solid) as a function of the eddy
 1044 viscosity depth scale, where $A_v(z) = A_{v0}e^{z/h_{Av}}$. Values are normalized by (29). Also plotted is the scaling
 1045 suggested by (30) (dashed), which overlaps the numerical solution for most of the parameter space.



1046 Fig. B1. Vertical structure of A_v models considered in Appendix B. In each case the normalization is such
 1047 that $h = 1$, $f = 1$, and $A_{v0} = Ek \times 1 \text{ m}^2 \text{ s}^{-1}$.



1048 Fig. B2. Accuracy of WKB approximation as a function of Ekman number for the A_v profiles shown in figure
 1049 B1. Top panel is for wind-forcing, bottom panel for a vertically uniform horizontal buoyancy gradient. Errors
 1050 are normalized according to (B5).